

2014

High-Resolution Sediment Records of Seismicity and Seasonal Sedimentation from Prince William Sound, Alaska, using XRF Core Scanning

Eric J. Miller

College of William and Mary - Virginia Institute of Marine Science

Follow this and additional works at: <https://scholarworks.wm.edu/etd>



Part of the [Geology Commons](#), [Oceanography Commons](#), and the [Sedimentology Commons](#)

Recommended Citation

Miller, Eric J., "High-Resolution Sediment Records of Seismicity and Seasonal Sedimentation from Prince William Sound, Alaska, using XRF Core Scanning" (2014). *Dissertations, Theses, and Masters Projects*. Paper 1539617947.

<https://dx.doi.org/doi:10.25773/v5-6bav-8b54>

This Thesis is brought to you for free and open access by the Theses, Dissertations, & Master Projects at W&M ScholarWorks. It has been accepted for inclusion in Dissertations, Theses, and Masters Projects by an authorized administrator of W&M ScholarWorks. For more information, please contact scholarworks@wm.edu.

High-Resolution Sediment Records of Seismicity and Seasonal Sedimentation from
Prince William Sound, Alaska, using XRF Core Scanning

A Thesis

Presented to

The Faculty of the School of Marine Science

The College of William and Mary

In Partial Fulfillment

of the Requirements for the Degree of

Master of Science

by

Eric J. Miller

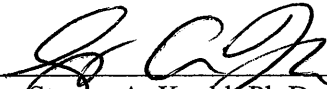
2014

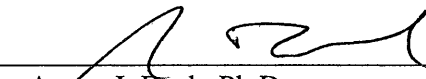
APPROVAL SHEET

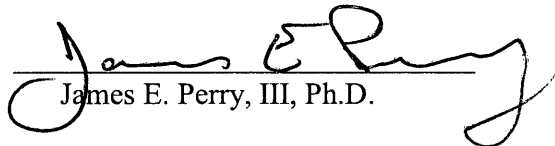
This thesis is submitted in partial fulfillment of
the requirements for the degree of
Master of Science


Eric J. Miller

Approved, by the Committee, August 2007


Steven A. Kucht, Ph.D.
Committee Chairman/Advisor


Aaron J. Beck, Ph.D.


James E. Perry, III, Ph.D.



Timothy M. Dellapenna, Ph.D.
Texas A&M University
Galveston, Texas

TABLE OF CONTENTS

	Page
ACKNOWLEDGMENTS	vi
LIST OF TABLES	vii
LIST OF FIGURES	viii
ABSTRACT	x
INTRODUCTION	2
BACKGROUND	5
Study Area	5
Geological Setting.....	5
Prince William Sound	7
Alaska Coastal Current	8
Climatic Setting	10
River Discharge	11
Methodology	12
²¹⁰ Pb	13
¹³⁷ Cs	13
X-Ray Fluorescence Core Scanning	14
METHODOLOGY	17
Core Collection	17
Core Processing	17
Photography	17
	iii

X-Radiography.....	18
Subsampling.....	18
Laboratory Analysis.....	19
Grain Size.....	19
²¹⁰ Pb Gamma Spectroscopy	19
²¹⁰ Pb Alpha Spectroscopy	20
¹³⁷ Cs Gamma Spectroscopy	22
X-Ray Fluorescence Core Scanning	23
RESULTS	24
Core Descriptions.....	24
Spatial Trends	24
Grain Size.....	25
Spatial Trends	25
Geochronology.....	26
Spatial Trends	27
X-Ray Fluorescence Core Scans.....	27
K/Ca	28
Sr/Pb.....	29
Br/Cl.....	30
DISCUSSION	31
Depositional Trends and Sediment Sources	31
XRF Proxies.....	35
K/Ca – Sediment Source.....	35

Sr/Pb – Grain Size.....	36
Br/Cl – Marine Organic Matter.....	37
Gravity Flow Deposits	38
1964 Gravity Flow Deposits	39
1983 Gravity Flow Deposits	41
1912 and 1890 Gravity Flow Deposits	44
Seasonal Sediment Deposits	45
Grain Size.....	46
Marine Organic Matter	49
CONCLUSIONS	52
LITERATURE CITED	54
 ELECTRONIC APPENDIX 1 – CORE PHOTOGRAPH AND X-RADIOGRAPH	
MOSAICS	
 ELECTRONIC APPENDIX 2 – GRAIN SIZE DATA	
 ELECTRONIC APPENDIX 3 – ²¹⁰Pb AND ¹³⁷Cs DATA	
 ELECTRONIC APPENDIX 4 – XRF DATA	

ACKNOWLEDGMENTS

I wish to thank my advisor, Dr. Steven A. Kuehl, as well as my committee members, Dr. Timothy M. Dellapenna, Dr. Aaron J. Beck, and Dr. James E. Perry for their guidance, support, and encouragement throughout the course of this project and my graduate education. I wish to thank Mary H. Goodwyn for her assistance in field work preparation and laboratory analysis. I wish to thank David and Annette Janka from the *M/V Auklet*, for their assistance in the retrieval of the sediment cores used in this study. I also wish to thank my family and friends for their continued support as well for making VIMS an unforgettable experience.

Financial assistance provided by NSF Grant OCE-1241185.

List of Tables

Table	Page
Table 1: Coordinates and water depths of the Prince William Sound gravity cores.	62
Table 2: Core averaged sand, silt, clay percentages, D50, and mean grain size.....	64
Table 3: ^{210}Pb and ^{137}Cs sedimentation rates.	66
Table 4: Core P-12 XRF correlations.	68
Table 5: Core P-7 XRF-Grain Size correlations.	70
Table 6: Core P-8 XRF-Grain Size correlations.	72
Table 7: Core P-9 XRF-Grain Size correlations.	74
Table 8: Core P-12 XRF-Grain Size correlations.	76

List of Figures

Figure	Page
Figure 1: Accretionary terranes of the study area.....	78
Figure 2: Surficial geology of Prince William Sound and Copper River basins	80
Figure 3: Prince William Sound bathymetry and coring locations.....	82
Figure 4: Flow pathway of Alaska Coastal Current.....	84
Figure 5: Monthly variations in Copper River discharge, the regional upwelling index, significant wave heights, and bottom wave orbital velocities for the Gulf of Alaska (Jaeger and Nittrouer, 2006).....	86
Figure 6: 2012 Copper River hydrograph and Cordova precipitation	88
Figure 7: Ephemeral redox colorations.....	90
Figure 8: Transect core mosaics	92
Figure 9: Non-transect core mosaics.....	94
Figure 10: Transect core averaged percentages of sand and clay	96
Figure 11: Prince William Sound core averaged percentages of sand, silt, and clay	98
Figure 12: Transect core sedimentation rates	100
Figure 13: Prince William Sound ^{210}Pb and ^{137}Cs radioisotope core profiles.	102
Figure 14: Core P-12 XRF profiles.....	104
Figure 15: Core P-10 XRF profiles.....	106
Figure 16: Core P-7 Sr/Pb - Grain size relationship	108
Figure 17: Core P-8 Sr/Pb - Grain size relationship	110
Figure 18: Core P-9 Sr/Pb - Grain size relationship.	112
Figure 19: Core P-12 Sr/Pb - Grain size relationship.	114
Figure 20: Core P-8 XRF profiles.....	116

Figure	Page
Figure 21: K and Ca streambed concentrations.	118
Figure 22: Historical earthquake epicenters.	120
Figure 23: Core P-9 XRF profiles.....	122
Figure 24: Core P-13 XRF profiles.....	124
Figure 25: Columbia Glacier ice damed lake levels (Krimmel, 2001).	126
Figure 26: Core P-7 Sr/Pb cyclicity.	128
Figure 27: Core P-8 annual redox thicknesses.....	130

ABSTRACT

The southern coast of Alaska is a climatically sensitive and tectonically active region, however due to its remoteness and harsh climate there are limited long-term historical records of environmental conditions such as storm frequency, river discharge, and earthquakes. In order to determine the potential for Prince William Sound sediments to contain high-resolution paleorecords of these conditions, a suite of 11 gravity cores was collected within the Sound in order to determine the modern day sediment depositional trends and to develop elemental proxies for earthquakes and seasonal sedimentation. $^{210}\text{Pb}/^{137}\text{Cs}$ -derived sedimentation rates and grain size trends indicate that there are two distinct sediment sources to the Sound; an allochthonous source of sediment that is advected into the Sound through Hinchinbrook Entrance, and an autochthonous source of sediment from the Columbia Glacier region of the northern Sound. Cyclic variations in grain size were identified in Hinchinbrook Entrance sediments using the XRF Sr/Pb ratio and were interpreted to be the result of seasonal sedimentation; with coarse-grained sediments deposited during the winter when storm-driven wave and currents in the nearshore region are high, and fine-grained sediments deposited during the summer when costal conditions are less energetic and when the discharge and transport of sediments from the Copper River is high. Additionally, light and dark colored laminations in northern Hinchinbrook Entrance sediments were interpreted to be the result of seasonal variations in the supply and preservation of organic matter; with high concentrations of organic matter preserved in the summer when primary production, the flux of terrestrial organic matter from rivers, and costal upwelling of potentially low oxygenated waters is high, and low organic matter concentrations preserved in the winter when primary production and river discharge are low, and when downwelling conditions likely introduce highly oxygenated waters. The use of the XRF Br/Cl ratio as a proxy for marine organic matter suggested that at least a portion of the dark, organic-rich, summer deposits had a marine origin, and may therefore be a potential proxy for seasonal sedimentation under certain conditions. Gravity flow deposits from the northern Sound were identified as having a source from the Columbia Glacier region using the XRF K/Ca ratio. The gravity flows that caused these deposits were identified as being triggered by historically recorded earthquakes, which likely remobilized sediment on the steep slopes of the northern channel and which then flowed downslope to the south. The results of this study indicate that the rapidly accumulating sediments in Hinchinbrook Entrance potentially contain high resolution records of Copper River discharge, storm activity and primary production, whereas sediments in the northern Sound may contain a regional seismic record.

High-Resolution Sediment Records of Seismicity and Seasonal Sedimentation from
Prince William Sound, Alaska, using XRF core scanning

INTRODUCTION

Continental margins are of both societal and scientific importance because they are regions of high population density, contain natural resources such as oil and gas, and preserve a record of environmental conditions on Earth. Continental margins mark the transition from continental to oceanic crust and are mainly composed of sediments eroded from land, but may also contain biogenic sediments formed in the overlying water column. The composition of continental margin sediments reflects the environmental conditions at the time of burial, therefore variations in composition with depth may be used to reconstruct paleorecords of these conditions. Active continental margins, such as the Pacific Margin, are formed by the subduction of oceanic crust, and are characterized by high seismicity, volcanism, and coastal mountain building (e.g., Lethcoe, 1999; Winkler, 2000). The relief and erodibility of these mountains results in large fluxes of terrestrial sediments and high burial rates along the margin (Milliman and Syvitski, 1992). Active margin sediments may therefore have the ability to preserve high-resolution records of local phenomenon such as earthquakes, storms, and river discharge.

High-latitude regions, such as Alaska, have been shown to be sensitive to climatic drivers such as the Arctic Oscillation and Pacific Decadal Oscillation, and are therefore ideal for reconstructing paleoclimatic records. These climatic conditions may be preserved in the sedimentary record as variations in the source, timing, and magnitude of sediment deposition. For example, during the winter of 2011-2012 the Arctic Oscillation was in its positive phase and the Prince William Sound (PWS) region of coastal Alaska experienced a record high 8.1m of snowfall (National Climatic and Data Center (NCDC), 2014). Two years later, during the winter of 2013-2014 the Arctic Oscillation was in its

negative phase, and the PWS region experienced record high temperatures (NCDC, 2014); which lead to unusually high winter snowmelt and river (sediment) discharge into PWS and the Gulf of Alaska.

In addition to being climatically sensitive, the southern coast of Alaska is one of the most seismically active regions in the world (Alaska Earthquake Information Center (AEIC), 2006). Nine out of the ten largest earthquakes within the United States have occurred in Alaska (United States Geological Survey (USGS), 2014A). Furthermore, in 1964 the world's 2nd largest earthquake (moment magnitude (M_w) 9.2) occurred in northern PWS, killing 131 people and causing 2.3 billion dollars (modern day equivalent) in property damage (USGS, 2014A). Since the 1960's the population of Alaska has more than tripled (United States Census, 2014), and billions of dollars have been spent on infrastructure, including the Trans-Alaskan Pipeline which terminates in Port Valdez (northern PWS) (Alyeska Pipeline, 2014).

In a period of both rapid population growth and natural and anthropogenically driven climate change, it is important to put such "record high" events in context with the long term past. However, reliable climatic and seismic records only go back to the 1900's. Therefore, in order to look at longer term trends it is necessary to develop paleoproxies for these conditions and to target areas where they will most likely be preserved.

Previous work on sediment dispersal and deposition along the Gulf of Alaska indicates that PWS is an area of rapid sediment accumulation, as evident by 100-200m thick Holocene sediment deposits (Carlson and Molnia, 1978; Milliman et al., 1996; Jaeger et al., 1998). Additionally, at least a portion of these sediments are likely from the

seasonal discharge of the Copper River (e.g., Naidu et al., 1976; Molnia and Hein, 1982; Klein, 1983; Milliman et al., 1996).

The objective of this study is to determine the potential for the sediments within PWS to contain high-resolution records of tectonics and climate. This will be accomplished by 1) determining the modern (centennial) sediment depositional trends within PWS using grain size and radioisotope analysis on a suite of gravity cores and 2) developing potential elemental proxies for sediment source and seasonal sediment deposition using x-ray fluorescence core scanning.

BACKGROUND

Study Area

This study focuses on sediments within PWS, which is located along the south central coastline of Alaska (Figure 1). However, these sediments likely have a source from both the PWS and the Copper River basins; therefore background information on both these regions will be given in the following sections.

Geological Setting

The geological setting of southern Alaska has largely been shaped by tectonic processes operating on a collision margin. Current-day Alaska is composed of a number of accretionary terranes sutured together along faults lines. These allochthonous terranes were transported to their present locations by subducting oceanic plates. Due to similar densities with the pre-existing Alaskan landmass, these terranes were accreted to the continent instead of being subducted underneath it. Within the regions of interest for this study, the upper Copper River basin is composed of the Wrangellia Composite Terrane, whereas the lower Copper River basin and PWS basin are composed of the Chugach Terrane and Prince William Sound Terrane (Figure 1). The different geological histories of these terranes have resulted in different rock compositions between the PWS and Copper River basins.

Within the PWS basin, the Prince William Sound Terrane encompasses the majority of the area adjacent to the shoreline of the Sound, and is composed of Eocene Orca Group rocks which can be generally described as sedimentary rocks composed of

turbidite sequences of sandstone, siltstone, and mudstone, with local outcrops of basalt and granite (Winkler, 2000) (Figure 2). Additionally, within the PWS basin, the Chugach Terrane surrounds the Prince William Sound Terrane and is composed of Valdez Group rocks, which can be described as a deformed flysh of metasedimentary (metasandstone, metasilstone, argillite, slate, and phyllite) and metavolcanic (metabasalt and metatuff) rocks (Winkler and Plafker, 1993).

The spatial extent of Orca and Valdez Group rocks continues westward from PWS into the lower Copper River basin. However, Valdez group rocks to the east of the Copper River are of higher metamorphic grade and include schists (pelitic schist and minor amphibolite), and gneiss (muscovite-biotite-quartz-plagioclas schist, banded gneiss, and migmatite), locally invaded with plutons of granite and granodiorite (Winkler and Plafker, 1993).

In comparison to the PWS and the lower Copper River basins, the upper Copper River basin is largely composed of the Wrangellia Composite Terrane; which comprises the Wrangell-St. Elias Mountains. This terrain is largely composed of a 3,000m thick Triassic basaltic greenstone overlain by nearly 1,000m of Triassic limestone and dolomite (Winkler, 2000). The basement rocks of the Wrangellia Composite are composed of andesite overlain by marine shale, sandstone, and limestone, and are invaded with large plutons of granite, monzonite and syenite (Winkler, 2000). Additionally, volcanic activity has resulted in large portions of the western Wrangell Mountains being overlain by andesite (Winkler, 2000).

The tectonic deformation associated with the current day collision and subduction of the Pacific Plate results in high seismic activity along the southern coast of Alaska. The AEIC (2006) estimates that 11 percent of the world's earthquakes occur along the southern coast of Alaska; including three out of the ten largest earthquakes ever recorded. The world's second largest earthquake (M_w 9.2) occurred on March 27, 1964 in northern PWS. Tectonic deformation associated with the 1964 Earthquake encompassed an area of 170,000-200,000 km² (Plafker, 1965). The average uplift for the PWS and the Copper River delta was 2m, however uplift as high as 10m occurred locally on Montague Island in southwest PWS (Plafker, 1965).

The crustal displacement and associated ground shaking from high magnitude earthquakes may result in submarine slope failure along steeply sloping fjords and channels. For example, the 1964 Earthquake triggered submarine slumping of unconsolidated alluvial and glacial sediments along the margins of fjords in northern PWS (Plafker and Mayo, 1965). Slumping may also result in the formation of gravity currents, which travel downslope before being deposited. For example, Carlson et al. (1978) suggests that turbidites within the Bering Trough may have been the result of earthquake-initiated gravity flows.

Prince William Sound

PWS is a large (~60km by 90km), semi-enclosed basin located along the south central coast of Alaska. The rugged and irregular shoreline of PWS has largely been shaped by ice and as a result contains many deep embayments and fjords. PWS continues to receive water and sediment from current day tidewater and mountain

glaciers. The largest glacier within PWS is the Columbia Glacier; which is a large (1,100 km²), rapidly retreating tidewater glacier located along the north central shoreline (Krimmel, 2001).

The bathymetry of PWS reveals that there is a large (11-16 km in width) submarine channel that extends from northern PWS south to Hinchinbrook Entrance (Figure 3). Within the Sound, this “central channel” is significantly deeper than the adjacent regions, reaching depths of >400m. However, approaching Hinchinbrook Entrance from the north maximum water depths decrease to 200m. Holocene sediment thicknesses, as determined by seismic profiles, reach 200m in the central channel near Hinchinbrook Entrance (Carlson et al., 1982; Milliman et al., 1996; Jaeger et al., 1998). Using these profiles from Hinchinbrook Entrance, Carlson and Molnia (1978) identified foreset beds dipping into PWS, which indicate an advection of sediment into the Sound. The clay mineralogy of this sediment suggests a source from the Copper River, which discharges into the Gulf of Alaska ~100km to the east (e.g., Naidu et al., 1976; Molnia and Hein, 1982; Klein, 1983; Milliman et al., 1996). Additionally, a Copper River source is supported by satellite images that have captured the Copper River’s surface plume entering PWS through Hinchinbrook Entrance (Feely et al., 1979; personal observations). Suspended sediment from the Copper River mouth is transported to PWS by the Alaska Coastal Current.

Alaska Coastal Current

The Alaska Coastal Current (ACC) is a year-round wind- and buoyancy-driven current that flows westward from British Columbia to Unimak Pass in the Aleutian

Islands (e.g., Royer, 1979; Johnson et al., 1988; Stabeno et al., 2002). The buoyancy induced (baroclinic) transport of the ACC is driven by high levels of coastal precipitation which act as a line source of freshwater along the coast, resulting in an across-shelf baroclinic gradient with subsequent geostrophic flow towards the west (Royer, 1982). In addition, the Gulf of Alaska's dominant southeasterly winds deflect water onshore due to the Coriolis effect, resulting in an across-shelf barotropic gradient and subsequent geostrophic flow to the west, intense downwelling conditions throughout much of the year, and the confinement of the ACC to within ~20km of the coast (Royer, 1982).

The speed of the ACC is determined by the magnitudes of the baroclinic and barotropic gradients, which respond to seasonal variations in freshwater input and wind (Johnson et al., 1988). The baroclinic transport of the ACC is positively correlated to freshwater input and is typically greatest in late fall when precipitation reaches a maximum (Royer, 1982). However, the barotropic gradient is driven by southeasterly winds, which are strongest in the winter months due to the seasonal formation of the Aleutian Low (AL). Primary alongshore transport appears to be driven by the barotropic gradient, therefore the greatest surface current speeds are typically during winter months (Johnson et al., 1988; Royer et al., 1990).

East of the Copper River, the ACC is diverted offshore by Kayak Island and an anticyclonic gyre forms in its lee (Figure 4) (Feely et al., 1979). Residence times within this gyre are on the order of 1-2 weeks, which allows enough time for sediment entrained in the ACC to settle out (Royer, 1983). Off the Copper River mouth the ACC resumes its westward course, deflecting sediments towards PWS. At Hinchinbrook Entrance a portion of the ACC bifurcates northward into PWS, while the remainder of the ACC

follows a southeasterly course along Montague Island. The portion of the ACC that enters PWS is subsequently deflected to the west and exits PWS through Montague Strait where it rejoins the portion of the ACC that did not enter the Sound, and continues to flow southeast along the coast.

Climatic Setting

The climate of southern Alaska is largely controlled by the AL; a semi-permanent low pressure system that forms over the Gulf of Alaska during the winter months (Rodionov et al., 2005). This system controls atmospheric circulation over the gulf; spawning, intensifying, and steering Pacific storms and warm, moist, air masses towards the Alaskan coast (Stabeno et al., 2001). As these storms and air masses rise up the coastal mountains, they experience adiabatic cooling and the majority of the moisture contained within them is released as precipitation. Due to this orographic effect, coastal regions of southern Alaska experience up to 800cm of precipitation per year, whereas interior regions receive typically receive <30cm of precipitation per year (L'Heureux et al., 2004). Interannual variability in precipitation can be correlated to changes in the strength and position of AL, which are in turn influenced by climatic drivers such as the Arctic Oscillation and Pacific Decadal Oscillation (Overland et al., 1999; Hartman and Wendler, 2005; Milliman and Farnsworth, 2011).

In addition to precipitation trends, wind and storm conditions caused by the AL result in seasonal trends in significant wave heights and upwelling-downwelling conditions for the Gulf of Alaska. For example, Jaeger and Nittrouer (2006) found that significant wave heights were greatest during the winter months (Figure 5). Additionally,

the increase in southeasterly winds results in increased downwelling conditions. In contrast, during the summer months the AL is replaced by the North Pacific High and wind speeds along the Gulf of Alaska relax, resulting in lower wave heights and decreased downwelling (possible upwelling) conditions (Niebauer et al., 1994; Jaeger and Nittrouer, 2006).

River Discharge

The sizes of fluvial drainage basins located along the Gulf of Alaska are limited by coastal mountain ranges which block the majority of inland runoff. As a result, there are numerous small rivers that have watersheds contained within 100km of the coast (Royer et al., 1990). However, the Copper River is one of the few rivers that drains a large inland area, and as a result represents the largest single source of freshwater and sediment to the Gulf of Alaska (Brabets, 1996).

The physical characteristics of the Copper River have been described in detail by Brabets (1996) and are summarized in the following three paragraphs. The Copper River basin encompasses 63,000km², including portions of the Alaska Range, Talkeetna Mountains, Wrangell-St Elias Mountains, and Chugach Mountains. From these headwaters the River follows a southerly course, bisecting the Chugach Mountains before discharging into the Gulf of Alaska. Due to a combination of high coastal precipitation and easily erodible, uplifted rocks, the annual suspended sediment discharge for the Copper River is estimated to be 70 million short tons yr⁻¹; making it the largest river in Alaska and second largest river in North America in terms of suspended sediment load.

20-50% of the Copper River's suspended load is in the clay-sized fraction ($<4\mu\text{m}$), with 10% in the sand-sized fraction ($>63\mu\text{m}$) and the rest in the silt-sized fraction ($4-63\mu\text{m}$). Nearly the entire bed load from the upper basin is trapped at Miles Lake; a glacially formed lake located $\sim 50\text{km}$ up stream of the Copper River mouth. Therefore, the only bed load being discharged at the river mouth originates from the alluvial plains south of Miles Lake.

The Copper River experiences seasonal discharge due to snowpack melt, glacial melt, and rainfall from May-October. For the remainder of the year the River is covered with ice and discharge is minimal. In order to look at trends and drivers of summer discharge, the discharge of the Copper River for 2012 was plotted alongside precipitation from nearby Cordova (Figure 6). The hydrograph shows a sharp increase in discharge beginning in late spring, which is believed to be driven by melting of the winter snowpack. After the majority of the annual winter snowpack has melted; discharge is believed to be driven by both rainfall and glacial melt. In addition to the spring melt peak, there is typically a late fall (Sept-Oct) peak in discharge, which corresponds to high rainfall during these months. Monthly averaged long term discharge data compiled by Jaeger and Nittrouer (2006) (Figure 5) do not show individual peaks in discharge driven by rainfall and melting which vary year to year, but do confirm that seasonal (summer) discharge by the Copper River is a long term (decadal) trend.

Methodology

This study determined recent (~ 60 years) depositional trends within PWS using the radioisotopes ^{210}Pb and ^{137}Cs . In addition, sediment sources and seasonal deposits

were determined using x-ray fluorescence core scanning. The theory and documented examples of these techniques will be described in the following paragraphs.

²¹⁰Pb Sedimentation Rates

²¹⁰Pb ($t_{1/2} = 22.3$ yrs) has been used to quantify modern sedimentation rates (<100 years) in freshwater and marine environments (e.g., Krishnaswamy et al., 1971; Koide et al., 1972; Nittrouer et al., 1979), and has been successfully used on the Alaskan continental shelf, including areas within PWS (Jaeger et al., 1998). This method assumes that the flux of sediments to the seabed is steady and that sediment mixing is confined to a “surface mixed layer”; below which ²¹⁰Pb activities decrease logarithmically with depth until background (²²⁶Ra supported) activities are reached. Within this “region of radioactive decay”, sedimentation rates are calculated using the slope of the natural logarithm of excess ²¹⁰Pb with depth.

¹³⁷Cs Sedimentation Rates

¹³⁷Cs ($t_{1/2} = 30.17$ yrs) has been used as an independent check on ²¹⁰Pb-derived sedimentation rates (e.g., Krishnaswamy et al., 1971; Robbins and Edgington, 1975; Nittrouer et al., 1983/1984). ¹³⁷Cs is formed in nuclear reactors and nuclear weapon explosions and has been introduced in detectable quantities to the environment through atmospheric fallout since 1952; with peak fallout in the northern hemisphere occurring in 1964 (Ritchie and McHenry, 1990). Therefore, the depth of peak ¹³⁷Cs activity and the greatest depth of ¹³⁷Cs detection can be dated to 1964 and 1952, respectively. In the absence of deep physical mixing, these ¹³⁷Cs horizon depths should not be more than the

number of years since peak fallout, multiplied by the ^{210}Pb sedimentation rate, plus the depth of the surface mixed layer.

X-ray Fluorescence Core Scanning

X-ray fluorescence (XRF) spectroscopy has been widely used to determine elemental concentrations in sediment samples. The principle behind XRF analysis has been described in detail by Verma (2007) and is summarized below. As an atom of a particular element is irradiated with x-rays an inner shell electron is energized and ejected from its orbit. An outer shell electron then drops down to fill the vacancy left behind from the ejected electron and an x-ray with an energy characteristic of the element is emitted. By measuring the intensity of the emitted x-rays an elemental concentration can be calculated.

Standard XRF analysis requires a dry, homogeneous sample, with a flat surface, for irradiation. This is typically achieved by grinding the sample into a uniform powder and pressing it into a pellet, or encapsulating it into a fused bead. These procedures are time consuming, costly, and result in the partial or complete destruction of the sample. XRF core scanning was therefore developed to provide a rapid, high resolution, non-destructive analysis on the surface of a split sediment cores (Jansen et al., 1998).

Since its introduction, XRF core scanning profiles have been used to identify sedimentary structures such as turbidites, varves, and sapropels (e.g., Rothwell et al., 2006; Thomson et al., 2006; Gracia et al., 2010; Kylander et al., 2011); to identify sediment sources (e.g., Kujau et al., 2010); as a proxy for grain size (e.g., Cuven et al., 2010; Kylander et al., 2011); and as a proxy for marine organic matter (e.g., Thomson et al., 2006; Brown et al., 2007; Ziegler et al., 2008; Addison et al., 2013).

Commercially available XRF core scanners, such as the third generation Avaatech scanner used in this study, have the capability of measuring elements Al-U at spatial resolutions down to 0.1mm. The design of the Avaatech scanner has been described by Richter et al. (2006) and is summarized in the following paragraph. The Avaatech scanner consists of an x-ray generator and an x-ray detector connected by a hollow prism. This prism is lowered to the surface of the core and flushed with helium to prevent the absorption of x-rays by water vapor. X-rays are then emitted from the generator and strike the surface of the core at a 45 degree angle. The detector is then positioned at the reciprocal 45 degree angle to capture the emitted x-rays from the core surface. The computer automated scanner then moves along the surface of the core at specified step intervals. At each interval the scanner records the intensity of emitted radiation for a predetermined amount of time, typically 30 seconds, before moving on to the next interval.

In addition to the speed and ease of the analysis itself, the preparation of the sediment core surface is minimal, requiring only smoothing and application of a thin Ultralene ® film. The purpose of this film is to 1) reduce variations in surface roughness, 2) prevent desiccation of core during the analysis, and 3) prevent contamination of the core surface and prism.

The results of XRF core scans are typically reported as elemental intensities (net area or counts per second) and can only be considered qualitative due to down core variations in surface roughness and water content, which result in variations in the measured intensities. Of these variables, water content may have the largest effect on the accuracy and interpretation of XRF core scans. Water preferentially absorbs x-rays

emitted from elements with low atomic numbers due to their low excitation energies (wavelengths). The degree of absorption follows Moseley's Law and scales inversely with atomic number; with lighter elements more affected by water attenuation than heavier elements. Analyses using marine sediment cores have shown significant water attenuation for elements Al – Fe (Tjallingii and Rohl, 2007; Hennekam and deLange, 2012). Down core variations in water content (porosity) may therefore be observed in the profiles of these light elements. Additionally, a thin film of water pools underneath the Ultralene® film. Variations in the thickness of this water layer have been shown to correlate with grain size; with coarser sediment overlain by a thicker film of water (Hennekam and deLange, 2012). Therefore, variations in the intensities of lighter elements may also mirror down core variations in grain size.

To reduce the effects surface roughness and water content the results from XRF analysis are commonly reported as elemental ratios. While ratios may reduce variations due to surface roughness, as all elements may be expected to be affected in the same way (Richter et al., 2006), the use of a light element that is affected by water adsorption will still result in inaccurate profile, as one of the elements is always more affected by water attenuation than the other (Hennekam and deLange, 2012).

METHODOLOGY

Core Collection

Sediment cores were collected in PWS from 6/24/12 - 6/26/12 onboard the vessel *M/V Auklet*. Cores were retrieved using a custom-designed gravity corer that utilized an acrylic barrel (length-2m; inner diameter-8.5cm) with a core catcher. A transect of five sediment cores (P-7, P-8, P-9, P-10, and P-12) was collected from Hinchinbrook Entrance northward along the central channel (Figure 3; Table 1) in order to target areas containing the thickest Holocene sediment deposits. For comparison; two sediment cores (P-5 and P-6) were collected in Port Etches, an inlet to the east of Hinchinbrook Entrance; two sediment cores (P-3 and P-13) were collected approximately 20km and 10km to the east of the central channel respectively; and two sediment cores (P-1 and P-2) were collected in far eastern PWS near the mouth of Simpson Bay. Once onboard, the barrels were removed from the corer, cut in half for ease of handling, and shipped via air freight to the laboratory for processing.

Core Processing

Photography

Sediment cores were split in half lengthwise and immediately photographed using a Nikon® digital camera attached to a fixed point ~50cm above the surface of the core. Core images were edited and spliced together to form core mosaics using Adobe® Photoshop® software.

X-Radiography

Digital x-radiographs of the split sediment cores were obtained using a MiniXRay® HF100⁺ x-ray generator, a Toshiba® DR flat panel detector, and scil IPS® processing software. The generator was positioned ~50cm above the surface of the detector and the emission energy was set between 40-60keV, depending on the thickness and composition of the core, for an exposure of 0.2 seconds. Digital x-radiographs were edited and spliced together to form core mosaics using Adobe® Photoshop® software.

Subsampling

One half of each split sediment core was subsampled in bulk 3cm thick sections for grain size and radioisotope analysis, while the other half was wrapped in cellophane to prevent desiccation, and stored in a cold room for subsequent XRF analysis. To speed core analysis, the following sampling procedure was followed; from a depth of 0-30cm, 3cm thick subsamples were continuously extracted; from a depth of 30-100cm, 3cm thick subsamples were extracted followed by a 2cm gap; at depths greater than 100cm, 3cm thick subsample were extracted followed by a 4cm gap.

In addition to the bulk subsamples, higher resolution subsamples were taken at specific regions of interest within the core (e.g., coarse layers and gravity flow deposits) for grain size analysis.

Laboratory Analyses

Grain Size

Grain size distributions for select bulk and high-resolution subsamples were determined using a Malvern® Mastersizer 2000™ that utilized a Hydro 2000G wet dispersion unit. Sample preparation was as follows; an aliquot of sample (~10g) was ultrasonicated in 15ml of 10% sodium hexametaphosphate for 30min. The solution was then diluted with 200ml of reverse osmosis water in a 250ml cylindrical glass container. A magnetic stir bar was then added to the solution and the container was set on a stir plate. The stirring speed was then adjusted such that a strong vortex formed in the container. An aliquot of solution was then removed ~1/2 way down the container and ~1/4 way across the vortex using a pipette. The aliquot was then added to the Malvern® Mastersizer™ until the instrument's laser obscuration was within operating range. Grain size fractions were recorded as a percentage by volume and were divided into four categories; sand ($\geq 63\mu\text{m}$), silt ($\geq 4\mu\text{m}$ but $< 63\mu\text{m}$) and clay ($< 4\mu\text{m}$).

^{210}Pb Gamma Spectroscopy

Sedimentation rates for each core were determined by the decay of excess ^{210}Pb activity with depth. Briefly, wet bulk subsamples were homogenized, packed into 70ml petri dishes, sealed with electrical tape, and aged for at least 21 days to allow for ^{222}Rn and decay products ^{214}Pb and ^{214}Bi , to reach secular equilibrium with ^{226}Ra . Samples were then counted for ~24hrs on Canberra semi-planar intrinsic germanium detectors and were recorded by ORTEC® multichannel analyzers. Detector counts per second at specific emission energies were calculated using ORTEC® MAESTRO® software.

Total ^{210}Pb activity was calculated by obtaining a detector counts per second at ^{210}Pb 's 46.5keV emission energy and then correcting for sample self-attenuation of gamma rays, gamma decay yield, and detector efficiency. To correct for sample self-attenuation of gamma rays at the 46.5keV energy level, an attenuation correction factor (A) was calculated for each sample using the following equation (Cutshall et al., 1983);

$$A = \frac{\ln\left(\frac{T}{I}\right)}{\left(\frac{T}{I}\right) - 1}$$

Where T is the attenuated beam intensity, determined by counting the packed sample with a ^{210}Pb source on top for 350 seconds and subtracting the intensity of ^{210}Pb generated from within the sample, and I is the unattenuated beam intensity, determined by counting the ^{210}Pb source on top of an empty petri dish for 60 seconds.

An average ^{226}Ra activity was calculated in the same manner, except for the self-attenuation correction, using the gamma emissions of ^{214}Pb at 295keV and 352keV, and ^{214}Bi at 609keV. Excess ^{210}Pb activity was then calculated as the difference between total ^{210}Pb activity and the activity of ^{226}Ra .

The natural log of excess ^{210}Pb activity (total ^{210}Pb activity – supported ^{210}Pb activity) was plotted at the midpoint depth of each subsample using Grapher™ 7 software. Sedimentation rates (S) were calculated according to the following equation;

$$S = \frac{\lambda}{m}$$

Where λ is the ^{210}Pb decay constant, and m is the slope of the best fit line.

^{210}Pb Alpha Spectroscopy

If the amount of bulk subsample from a core was insufficient to fill the 70ml petri dish needed for gamma analysis, all samples from that core were analyzed for total ^{210}Pb

activity using alpha spectroscopy. This method calculated total ^{210}Pb activity by measuring the alpha decay of ^{210}Pb 's daughter isotope ^{210}Po , assuming secular equilibrium.

The method for alpha ^{210}Po analysis was similar to that of Nittrouer et al. (1979). Briefly, ~4g of dried and ground sediment was spiked with a known activity of ^{209}Po in order to determine procedural yield and to calculate the activity of ^{210}Po . Organic matter was then removed (oxidized) from the sediment by adding ~10ml concentrated HNO_3 and heating on a hot plate till dry. Particulate bound ^{210}Po was then released into solution by adding ~10ml of 6N HCl and digesting the solution in a Milestone ETHOS EZ Microwave oven. The digested sediment was then removed from solution by centrifugation. Ascorbic acid (5-10g) was then added to the solution to reduce Fe III to Fe II, before ^{210}Po and ^{209}Po were spontaneously plated onto silver planchets. The alpha emission from the planchets was then counted using an ORTEC® alpha detector for 24hrs. Detector counts per second at the emission energies of ^{210}Po (5264keV) and ^{209}Po (4843keV) were then determined using ORTEC® MAESTRO® software.

The activity of ^{210}Po (A_{210}) was then calculated according to the following equation;

$$A_{210} = \frac{C_{210}}{C_{209}} * A_{209}$$

Where C_{210} is the detector counts of ^{210}Po , C_{209} is the detector counts of ^{209}Po , and A_{209} is the known activity of ^{209}Po spike.

The natural log of total ^{210}Pb (^{210}Po) activity was then plotted at each midpoint depth using Grapher 7 software. The activity of supported ^{210}Pb was determined as the average activity of total ^{210}Pb in the region of the core where activity remained uniform

with depth. Excess ^{210}Pb activity for each subsample was then calculated by subtracting the supported ^{210}Pb activity from the total ^{210}Pb activity. Excess ^{210}Pb was then plotted at the samples midpoint depth and the slope of the best fit regression was used to calculate sedimentation rates in the same manner as described for gamma analysis.

^{137}Cs Gamma Spectroscopy

The depth of peak ^{137}Cs activity was used to validate ^{210}Pb sedimentation rates by independently calculating an average sedimentation rate for the time period between core collection and peak atmospheric fallout of ^{137}Cs in 1964. In addition to peak ^{137}Cs , the greatest depth at which ^{137}Cs was detected was also used to calculate an average sedimentation rate since 1952, as this was the first year that detectable quantities of ^{137}Cs were first introduced to the environment. ^{137}Cs activities of core subsamples were measured using the ^{210}Pb gamma spectroscopy method previously described. ^{137}Cs activity was calculated using the gamma emission of ^{137}Cs at the 661keV energy level. For cores where ^{210}Pb activity was measured by alpha emission, ^{137}Cs activity was determined by packing the dried and ground sample into a cylindrical vial (inner diameter x height = 19 x 48mm), and counting it on a Princeton Gamma-Tech germanium well detector. ^{137}Cs activity was plotted for each depth point using Grapher™ 7 software. Average sedimentation rates were then calculated by dividing the depth of peak ^{137}Cs and the greatest depth ^{137}Cs was detected by the number of years that have occurred from 1964 and 1952 respectively to the time of core retrieval.

X-Ray Fluorescence Core Scanning

X-Ray fluorescence core scans were obtained on the split sediment cores using a third generation AvaaTech XRF core scanner housed at the International Ocean Discovery Program facility at Texas A&M University, College Station. Core preparation included smoothing the core surface and covering it with a 4 μ m thick Ultralene® film. Cores were scanned at a 10kV irradiation energy to capture the emission of the elements Al, Si, P, S, Cl, Ar, K, Ca, Ti, Cr, Mn, Fe, Rh, and Ba, and at a 30kV energy to measure the elements Ni, Cu, Zn, Ga, Br, Rb, Sr, Y, Zr, Nb, Mo, Pb, and Bi. Scans were obtained at a 5mm spatial resolution. Each interval was scanned for 30 seconds and the emission intensity for each element was automatically recorded in a spreadsheet. Down core elemental profiles were edited and aligned with core mosaics using Grapher™ 7 software.

RESULTS

Core Descriptions

The following core descriptions are based on both visual observations of structure, texture, and color taken immediately after the sediment cores were split as well as observations from the corresponding x-radiographs. See Appendix 1 for individual core photograph and x-radiograph mosaics.

The sediment cores collected in PWS showed varying degrees of structure and color. In general, the cores were fine-grained, showed little structure, and were tan in color. However, specific cores contained regions with distinct structures (i.e., physical laminations and gravity flow deposits) and unique colorations. Interestingly, the surfaces of recently split sediment cores showed varying degrees of black colored pockets and black streaking across the width of the core. However, these black colorations were ephemeral and after being exposed to air overnight were no longer observed (Figure 7). Therefore, these black colorations are believed to be the result of reducing conditions and the formation of iron sulfides, which are rapidly oxidized after exposure to air, resulting in the observed color change.

Core Structure – Spatial Trends

The sediment cores that composed the central channel transect (P-7, P-8, P-9, P-10, P-12) showed a northward decrease in the degree of physical layering (Figure 8). Core P-7, which was retrieved from Hinchinbrook Entrance, showed distinct physical laminations composed of interbedded coarse and fine-grained layers. Core P-8, which was retrieved ~10km north of core P-7, also showed physical layering, however the

differences in grain size between coarse and fine-grained layers was less pronounced than core P-7. In addition to physical layering, uniformly spaced ephemeral light and dark colored laminations (“redox banding”) were observed throughout core P-8. Cores P-9 and P-10, which were retrieved ~15km and ~25km to the north of core P-7 respectively, displayed mottled textures throughout; except for a distinct gravity flow deposit in core P-9 that could be clearly identified by its sandy basal layer at 80cm. Core P-12, the northernmost core which was retrieved ~40km north of core P-7, also displayed a mottled texture throughout; except for two distinct gravity flow deposits with bases at 38cm and 70cm depths. The non-transect sediment cores (P-1, P-2, P-3, P-5, P-6, and P-13) generally showed mottled textures throughout (Figure 9); with the exception of a distinct gravity flow deposit in core P-13 with a base at 34cm.

Grain Size

See Table 2 core averaged grain size measurements, Electronic Appendix 2 for grain size measurements of select bulk and high resolution subsamples, and Electronic Appendix 1 for down core grain size profiles. The reported errors represent the standard error of the core averaged percentages.

Average Grain Size - Spatial Trends

Average grain size values for the central channel transect cores showed that the highest sand content was recorded for core P-7 ($21 \pm .9\%$) and progressively decreased northward in each core with a minimum sand content recorded for core P-12 ($1.1 \pm .3\%$) (Figure 10). Conversely, average percent clay content followed the opposite trend, with

minimum content recorded for P-7 ($23 \pm .5\%$) and maximum content recorded for P-12 ($38 \pm .8\%$).

The non-transect sediment cores can be spatially grouped in pairs for comparison to each other and to nearby central channel cores. The two cores (P-5, and P-6) retrieved from Port Etches had significantly lower sand contents ($4.8 \pm .3\%$ and $5.8 \pm .2\%$ respectively) than the two cores (P-7, and P-8) retrieved in the nearby central channel (Figure 11). The two cores (P-3 and P-13) retrieved from the east of the channel had varying sand and clay contents; core P-13, which was retrieved closer to the channel, was composed of $2.5 \pm .3\%$ sand and $36 \pm .7\%$ clay, while core P-3 contained a greater sand content ($12 \pm .6\%$) and a lesser clay content ($26 \pm 1\%$). The two cores (P-1, P-2) retrieved from far eastern PWS showed significantly different grain size fractions despite their close spatial proximity; core P-1 had the highest sand content ($22 \pm .9\%$) from any of the cores collected, while core P-2 had one of the lowest sand contents ($4.3 \pm .1\%$).

Geochronology

Due to an inadequate amount of subsample needed for gamma spectroscopy, the ^{210}Pb activities for cores P-1, P-2, and P-13 were measured by alpha spectroscopy while their corresponding ^{137}Cs activities were separately measured by gamma spectroscopy. For the remaining cores, ^{210}Pb and ^{137}Cs were simultaneously measured using gamma spectroscopy. See Table 3 for ^{210}Pb and ^{137}Cs sedimentation rates and associated errors. See Electronic Appendix 2 for detector data and individual core profiles.

Spatial Trends in Sedimentation Rates

Sedimentation rates along the central channel transect progressively decreased from a maximum rate of 4.4cm yr^{-1} at core P-7 to a minimum rate of 1.1cm yr^{-1} at core P-10 (Figure 12). From core P-10, the sedimentation rate increased slightly to 1.3cm yr^{-1} at core P-12.

In Port Etches, cores P-5 and P-6 had varying sedimentation rates (1.7cm yr^{-1} and 2.6cm yr^{-1} , respectively) despite their close proximity (Figure 13). Interestingly, the accumulation rates in Port Etches were approximately half that of accumulation rates from cores P-7 and P-8, which were retrieved in the adjacent central channel.

To the east of the central channel in central PWS, core P-13 had the lowest calculated sedimentation rate (0.3cm yr^{-1}) for all the PWS cores. Moving $\sim 10\text{km}$ to the east of core P-13, the sedimentation rates for core P-3 (0.7cm yr^{-1}), was approximately double the accumulation from core P-13. At the easternmost locations, core P-1 and P-2 had sedimentation rates (0.7cm yr^{-1} and 0.5cm yr^{-1} , respectively) that were similar to those of core P-3. In general, rates in the eastern shallow areas of PWS were lower than central channel cores.

X-Ray Fluorescence Core Scans

XRF core scans produced down core profiles of emission intensities for the 27 individual elements measured. In general, the profiles of lighter elements (Al-Fe) displayed signs of water attenuation, as seen through mirrored profiles with Cl (proxy for water content), and therefore must be interpreted with caution. When plotted alongside the core mosaics, specific elements and elemental ratios showed visual correlations to

grain size, sediment coloration, and redox banding. These visual trends provided the basis for high-resolution grain size sampling and the creation of correlation matrixes for specific core regions of interest, as detailed below. See Electronic Appendix 4 for raw XRF data.

K/Ca

Peaks in the K/Ca ratio corresponded to regions of fine-grained, grey-blue colored sediment in cores P-10 and P-12. In core P-12, four peaks in the K/Ca ratio were observed at: 32-38cm, 55-70cm, 120-129cm, and 140-149cm depths (Figure 14). As noted earlier, both K and Ca are significantly attenuated by water, as can be observed both visually in the mirrored profile of K and Ca with Cl (proxy for water content) in core P-12, and statistically in the negative correlation between K-Cl ($r = -.87$) and Ca-Cl ($r = .81$) in regions of the core where peaks in the K/Ca ratio are not observed. Because K is affected by water attenuation to a greater degree than Ca, due to its lower atomic mass, a peak in the K/Ca ratio may be driven by a decrease in water content. While a decrease in water content (Cl) is observed for the four peaks in K/Ca in core P-12, the correlations between K-Cl and Ca-Cl (Table 4) within these peak regions suggests that they represent actual deviations in elemental concentrations. For example in the K/Ca peak from 32-38cm, Cl intensities decrease which results in a predictable increase in the intensity of K. However, for the same interval Ca concentrations do not increase, but instead decrease. If the peak in K/Ca was only caused by water attenuation it would be expected that Ca concentrations would have also increased. The result of increasing K and decreasing Ca is a significant peak in the K/Ca profile. Similar K and Ca trends can

be observed in the remaining K/Ca peaks in core P-12. Additionally, two similar peaks in K/Ca corresponding to grey-blue sediment were observed in core P-10 from 25-28cm and 43-49cm (Figure 15).

Sr/Pb

High-resolution grain size measurements from cores P-7, P-8, P-9, and P-12 exhibited statistical correlations with XRF intensities for select elements (Tables 5, 6, 7, 8). Across all cores, Sr displayed a strong positive (negative) correlation with coarser (finer) grain sizes; while Pb displayed the opposite correlations. Furthermore, the Sr/Pb ratio also showed a positive correlation with grain size. However, the correlations between Sr/Pb and different grain size fractions (sand, silt, and clay) varied between cores. For example, in cores P-7 and P-8, Sr/Pb showed a strong positive correlation with sand, and a strong negative correlation with silt and clay (Figures 16, 17). This was due to a large increase (decrease) in the percentage of sand (silt and clay) in the coarse layers. In contrast, Sr/Pb in core P-9, showed a strong positive correlation to sand; no correlation to silt; and a strong negative correlation to clay (Figure 18). This was due to the percentage of silt remaining fairly consistent while the fractions of sand and clay varied inversely to one another. However, in core P-12, Sr/Pb showed a poor correlation with sand and a strong correlation with silt and clay (Figure 19). This was caused by a low percentage of sand, which resulted in grain size variations being driven by changes in the silt and clay fractions.

While the Sr/Pb relationship between grain size fractions varies depending on the core, and likely the specific core interval, the overall correlation between Sr/Pb and

relative grain size is observed across all the cores, which can be seen in positive correlation between Sr/Pb and the mean grain size (Figures 16-19).

Br/Cl

In general, peaks in the XRF Br/Cl ratio visually correlated with the uniform redox banding in the core photograph of P-8 (Figure 20). The Br/Cl ratio is a function of water content (Cl), which appears to be influenced by high percentages of sand. For example, sandy layers from 38-44cm, 52-64cm 72-74cm, and 80-84cm had abnormally high Cl values, which significantly decreased the Br/Cl ratio. This increase in Cl within sandy intervals is likely due to the pooling of water underneath the Ultralene® film.

Variations in the Br/Cl ratio due to variations in the water film thickness appear to be limited to the upper 95cm of core, as this is where the majority of the sandy layers are contained. This can be observed statistically through the negative correlation ($r = -.84$) between Br/Cl and Sr (proxy for coarse sediments) for this region of the core. In the lower portion of the core, variations in grain size appear to be less pronounced and do not contain significantly sandy intervals. Furthermore no significant correlation ($r = .10$) was found between Sr and Br/Cl, therefore variations in water film thickness do not appear to drive the Br/Cl ratio in the lower portion of core P-8.

DISCUSSION

Depositional Trends and Sediment Sources

The observed decrease in both core-averaged grain size distributions and sedimentation rates along the central channel transect from core P-7 to core P-10 (Figure 10 and 12) suggests an advection of allochthonous sediment into PWS through Hinchinbrook Entrance. The decrease in the core averaged percentage of sand-sized sediments northward from core P-7 to core P-10 suggests that upon entrance to the Sound, larger sediments with faster settling velocities are deposited closer to Hinchinbrook Entrance. The increase in the core averaged percentage of clay from core P-7 to core P-12 suggest that finer sediments, with slower settling velocities, are advected further northward into the Sound before being deposited. Additionally, the decrease in sedimentation rates from core P-7 to core P-10 supports the idea that Hinchinbrook Entrance acts as a large point source of sediment for the southern portion of the Sound; as higher sedimentation rates were calculated nearer to the source. The slight increase in sedimentation rate from core P-10 to core P-12, the northernmost core of the central channel transect, suggests an additional autochthonous source of sediment to the Sound. This sediment may be from the numerous small streams and rivers that drain directly into northern PWS. In Addition, the Columbia Glacier has been suggested as a large source of sediment to the northern Sound (Milliman et al., 1996).

Low sedimentation rates and low percentages of sand sized sediments for cores P-5 and P-6, compared to cores P-7 and P-8 (Figure 11 and 13), suggest that Port Etches is bypassed by the majority of sediment being advected into PWS. This is supported by

both current measurements and numerical models which that indicate that the greatest flux of water into the Sound occurs on the western side of Hinchinbrook Entrance (Niebauer et al., 1994; Wu, 2011; Halverson et al., 2013).

Likewise, a low sedimentation rate calculated for core P-13 suggests that the region to the east of the channel in central PWS does not receive significant amounts sediment advected into the Sound through Hinchinbrook Entrance (Figure 13). This is likely due to the general southwesterly surface flow within the Sound (Royer et al., 1990), which would deflect sediment Entering PWS through Hinchinbrook Entrance away from coring location P-13. In addition, the greater water depths of the central channel (>400m), compared to the depths near coring location P-13 (<150m), would allow suspended sediment to be advected further northward into the Sound before being deposited, as greater water depths allow for increased particle settling time and northward transport time. Furthermore, once sediment has settled below 150m, it would be trapped within the margins of the channel, assuming upwelling within the Sound insignificant, and would not spread laterally to the east.

To the east of coring location P-13, an increase in the sedimentation rate and core averaged percentage of sand for core P-3 suggests an easterly source of sediment for this region of the Sound (Figure 13). Further to the east, cores P-1 and P-2 show the spatial variability in both sedimentation rate and grain size that can occur proximal to the shoreline (Figure 11 and 13). The sediment that composes cores P-1 and P-2 is likely a combination of allochthonous sediment from the Copper River, which enters the eastern portion of the Sound between the mainland and Hawkins Island, as well as an

autochthonous source of sediment from within the Sound, such as the glacial fed streams that drain directly into the head of nearby Nelson Bay (Figure 3).

While the spatial trends in grain size and sedimentation rates described above indicate an advection of allochthonous sediment into the Sound through Hinchinbrook Entrance, the size of sediments observed in the coarse-grained layers from cores P-7 and P-8 are too coarse to be directly transported from the mouth of the Copper River to Hinchinbrook Entrance as part of the Copper River's suspended sediment plume. For example, the mean grain size taken from a coarse-grained interval in core P-7 (118-119cm) was $\sim 108\mu\text{m}$. Based on Stokes settling equation, a particle of this diameter will have a settling rate of 0.66m/s. Assuming a nearshore depth of 60m, this particle would have settled in 91 seconds in the absence of turbulence. At a surface current speed of 100 cm/s (typical for the ACC), it would take surface plume sediment over 24hrs to travel $\sim 100\text{km}$ from the mouth of the Copper River to coring location P-7 at Hinchinbrook Entrance. Therefore it is unrealistic that the coarse sediments found at Hinchinbrook Entrance were transported from the mouth of the Copper River without first being deposited in the nearshore region.

If the sand sized sediments found at Hinchinbrook Entrance were not transported as part of the Copper River's sediment plume, then they likely have a proximal source from Hinchinbrook Island, Montague Island, or the nearshore region to the east of Hinchinbrook Entrance. Having a source from Hinchinbrook Island is unlikely as coarse-grained layers comparable to those in cores P-7 and P-8 were not observed in cores P-6 and P-5, which were collected upslope and nearer to Hinchinbrook Island (Figure 3). Montague Island is also a possible source, however due to the dominant flow of currents

into the Sound on the western side of Hinchinbrook Entrance, and a subsequent deflection of the current to western portion of the Sound, it is unlikely that the dominant transport direction of suspended sediment from Montague Island would be towards core P-7. Additionally, the bathymetry of Hinchinbrook Entrance would suggest that any sediments being transported downslope from Montague Island, as part of the bed load, would be trapped in the 300m+ depression that divides Montague Island and core P-7.

The coarse sediments observed in cores P-7 and P-8 therefore likely have an immediate source from the nearshore region to the east of Hinchinbrook Entrance. Sediment characterization of this region by Carlson et al. (1977) revealed that sand is contained within the nearshore region to a depth of ~60m. The sand-mud transition approximately follows the 60m isobath which extends around the southernmost point of Hinchinbrook Island. From this point the seabed slopes down to coring locations P-7 and P-8. It is believed that coarse sediments are transported from this nearshore location to deeper depths within Hinchinbrook Entrance during the winter months when both current and wave action are annually highest (Johnson et al., 1988; Jaeger and Nittrouer, 2006).

The absence of normally graded coarse layers suggests that these coarse grains are not transported downslope to the coring locations through gravity flows. Furthermore, the slope of the seabed between cores P-7 and P-8 ($<1^\circ$) is not great enough to produce auto suspending gravity flows and the water depths ($>200\text{m}$) are too great for wave supported gravity flows. However, the rapid settling velocities (in the absence of turbulence) of the largest sediments observed in cores P-7 and P-8 suggest that they cannot be resuspended from the nearshore region and transported to the coring locations without first being deposited. Therefore it is believed that these coarse grains are.

transported as part of both the suspended load and current driven bed load. However, the contribution from each of these pathways is unknown.

In addition to allochthonous sediment that enters the Sound to the south, a northerly autochthonous source of sediment is suggested by a slight increase in the sedimentation rate from core P-10 to core P-12 (Figure 12). The sediment that composes core P-12 is fine-grained (Figure 10) and may therefore be easily transported as part of the suspended load. However, the presence of gravity flow deposits in cores P-10 and P-12 (discussed in detail in the following sections) indicates that at least a portion of this sediment was episodically transported through gravity flows.

XRF Proxies

The XRF K/Ca, Sr/Pb, and Br/Cl ratios were used as proxies for sediment source, grain size, and marine organic matter respectively. These proxies proved valuable in the interpretation of sediment depositional trends within PWS and are described in detail below.

K/Ca – Sediment Source

The K/Ca ratio may be used as sediment source indicator in certain settings as K is typically enriched in felsic rocks and depleted in mafic rocks, while Ca shows the opposite trends and is typically enriched in mafic rocks and depleted in felsic rocks. In cores P-10 and P-12, peaks in the K/Ca ratio corresponded to regions of the core that were composed of grey-blue colored sediment (Figure 14 and 15). Both the elevated K/Ca values and unique coloration are believed to be identifying features of sediment

sourced from the Columbia Glacier region of PWS. In contrast, the background sediment contained in these cores, which has low K/Ca values and a tan coloration, is believed to have a dominant source from the Copper River basin.

Elemental concentrations of streambed sediments analyzed from the PWS and Copper River basins by the USGS indicate that K (Ca) is enriched (depleted) in the Columbia Glacier region of PWS compared to sediments taken from adjacent regions of the Sound and the Copper River basin (USGS, 2013). In contrast Ca (K) appears to be enriched (depleted) in sediments from the upper Copper River basin (i.e., Wrangell Mountains) (Figure 21). These spatial trends in elemental concentrations are likely driven by the geological differences between the two regions. For example, the Prince William Sound basin is generally composed of meta-sedimentary rocks, whereas the upper Copper River basin contains volcanic rocks. The elemental composition of these riverine sediments suggests that they are indicative of their provenance. Therefore, the K/Ca may be useful in differentiating northern PWS-Columbia Glacier sediment from Copper River sediment.

Sr/Pb – Grain Size

The positive correlations between Sr and grain size for the PWS cores discussed earlier (Tables 5-8) are similar to observations made by Zhang et al. (2002) from Bohai Bay, China, and Kylander et al. (2011) from Lake Les Echets, France. These studies concluded that Sr was associated with plagioclase feldspar minerals that were likely enriched in the coarser, less chemically-weathered grains. In comparison, increased chemical weathering in finer grains likely results in the dissociation of Sr containing

minerals. The watersheds draining into PWS and the nearby Gulf of Alaska are small, mountainous, and typically contained within 100 km of the coast (Royer et al., 1990). Sediment residence times within these basins are short (Milliman and Syvitski, 1992), therefore the coarse-grained sediments discharged at the coast may be composed of chemically-unweathered minerals. Therefore, the observed relationship between Sr and grain size observed in the PWS region is reasonable.

In contrast to Sr, Pb XRF intensities displayed a negative correlation to grain size (Tables 5-8). Similar relationships between Pb and grains size have been commonly recorded in riverine and coastal sediments (e.g., Whitney, 1975; Thorne and Nickless, 1981; Cauwet, 1987; Horowitz and Elrick, 1987; Borovec, 2000). The enrichment of Pb in the fine-grained sediments of PWS is likely the result of an increase in the total sediment surface area, however it is unknown whether Pb is binding to the surface of the particle itself, or to surface coatings such as manganese oxide, which may increase Pb scavenging, and which may be enriched in the fine-grained fraction.

To investigate down core variations in grain size the Sr/Pb ratio was used because Sr and Pb displayed opposite correlations to grain size. The Sr/Pb ratio should therefore allow for small changes in grain size to be magnified. Additionally, the use of the Sr/Pb elemental ratio reduces measurement artifacts due to down core variations in surface roughness, as both Sr and Pb are assumed to have the same response to these variations.

Br/Cl – Marine Organic Matter

Br has been successfully used as a proxy for marine organic matter in XRF core scanning studies, including locations along the southeast coast of Alaska (Thomson et al.,

2006; Ziegler et al., 2008; Addison et al., 2013). Br is enriched in marine organic matter relative to terrestrial organic matter (Mayer et al., 2007; Ziegler et al., 2008); however Br is also a conservative constituent of seawater (Morris and Riley, 1966). In order to focus on organically bound Br, Br was normalized by water content. Cl concentrations in organic matter and within the sediment grains themselves is generally insignificant in comparison to the amount of Cl dissolved in seawater, therefore the XRF intensity of Cl may be used as a proxy for water content (Tjallingii and Rohl, 2007; Hennekam and deLange, 2012). Therefore by normalizing Br by Cl, the response of dissolved Br is reduced.

Gravity Flow Deposits

Rapid sediment accumulation and steep bathymetry make regions within PWS susceptible to slope failure and the formation of gravity flows (Plafker, 1965). Furthermore, slope failures in PWS may be triggered earthquakes (Plafker, 1965; Carlson et al., 1978). In addition to earthquake initiated slope failures, gravity flows may be formed by glacial outburst floods if the suspended sediment concentrations within the flood waters are great enough for hyperpycnal flows to form upon contact with water from the Sound (Mulder, 1995). In the following paragraphs, the likely triggers of the gravity flow deposits observed in the PWS sediment cores will be discussed based on the core's geochronology and available data on historic earthquakes and glacial outburst floods. Furthermore, the likely sources and pathways of the gravity flows will be evaluated using physical and geochemical evidence from the gravity flow deposits and the general bathymetry of the Sound.

1964 Gravity Flow Deposits

The gravity flow deposits observed in cores P-9, P-12 (70cm base), and P-13 (Figures 14, 23, and 24) can be dated to 1964 based on peak ^{137}Cs activity, and are interpreted to have been triggered by the March 27, 1964, Great Alaskan Earthquake (M_w 9.2), which had its epicenter located in northern PWS (Figure 22). In addition to these 1964 gravity flow deposits, which were identified based on their erosive bases and fining-upward sequences, a unique sediment interval from 43-49cm was identified in core P-10 that also dates to the same time period based on ^{137}Cs geochronology (Figure 15). Similarities in color and the relative down core K/Ca ratio between the 1964 intervals in cores P-10 and P-12 suggest a similar sediment source. Based on the high K/Ca signature of these deposits, this source is likely the Columbia Glacier region of northern PWS.

In addition to a K/Ca geochemical signature, variations in the physical structure between the 1964 deposits in core P-10 and P-12 are consistent with a gravity flow originating at the head of the central channel in the Columbia Glacier region. Core P-12 was collected closer to the Columbia Glacier and its 1964 gravity flow deposit is composed of a distinct 3cm thick basal unit of coarse, silt-sized sediments followed by a ~7cm thick fining-upward unit (Figure 14). In comparison, the 1964 gravity flow deposit in core P-10, which was retrieved ~20km south of core P-12, was diffuse in color and structure, and did not show a distinct coarse basal unit in the x-radiograph (Figure 15). High-resolution grain size measurements from within the this deposit are not available, however based on the Sr/Pb ratio, the deposit was composed of a ~6cm thick fining-upward sequence, which suggests that it was produced by a gravity flow. The decrease in the thickness and coarseness of the 1964 deposit from core P-12 to core P-10 is consistent

with a gravity flow originating at the head of the central channel and rapidly traveling down slope to coring location P-12, where the coarsest sediment was deposited, and then continuing to run out southward along the bottom of the channel to coring location P-10, where the finest sediment settled out as a diffuse deposit.

Furthermore, the fine-grained composition of the 1964 deposit in core P-10 suggests that the gravity flow did not travel down the steep western slope of the central channel immediately adjacent to the coring location. If the gravity flow had travelled down this western slope, its speed would likely have been great enough to transport and deposit coarser sediment similar to the gravity flow deposits in cores P-9 and P-13. Furthermore, the seabed gradients upslope of coring locations P-9 and P-13 were less than the gradient to the west of P-10.

The lack of peak K/Ca values in the gravity flow deposits in cores P-9 and P-13 (Figures 23 and 24) suggest that their corresponding gravity flows had different sources and transport pathways than the gravity flows responsible for the P-10 and P-12 deposits. The seabed gradient at coring location P-9 (Figure 3) suggests that the gravity flow originated towards the south and traveled northward. Additionally, the thick sandy basal unit of the core P-9 deposit supports this southerly source, as the highest percentages of sand sized sediments were found in cores to the south of P-9.

The gradient of the seabed surrounding P-13 suggest that the gravity flow responsible for the observed deposit originated towards the north and traveled downslope towards the south. While coring location P-13 is located in a trough between Hinchinbrook Island and northern PWS, the gradient to the north is greater than the gradient to the south and would therefore be more prone to slope failure and the

formation of a gravity flow. Furthermore the northern slope was closer to the 1964 Earthquake epicenter and would therefore be expected to receive more intense seismic shaking that would likely produce a slump and gravity flow in comparison to the southern slope. The lack of a K/Ca peak in this deposit suggests that the sediment contained on the northerly slope does not have a source from the Columbia Glacier, and is therefore not the result of suspended sediment from the Columbia Glacier region being advected to the southeast. The general southwest currents observed by Royer et al. (1990) within the northern portion of the Sound suggest that the sediment on this northerly slope has a source to the east.

1983 Gravity Flow

In addition to the 1964 gravity flow deposit in core P-12, a gravity flow deposit from 34-38cm was clearly observed in both the core photograph and x-radiograph (Figure 14). This deposit was composed of a 0.5cm thick basal unit of silt, followed by a 3.5cm thick segment of grey-blue clay. The K/Ca profile showed a large peak corresponding to the fine-grained upper unit which suggests that this sediment has a source from the Columbia Glacier region. Based on the core's geochronology, this deposit occurred in the early 1980's. Two possible events that may have produce gravity flows emanating from the Columbia Glacier region during this time period are glacial outburst floods and earthquakes.

Outburst floods from two of the Columbia Glacier's ice dammed lakes, Lake Kadin and Lake Terentiev, have been recorded using aerial altimetry data since the 1976 (Krimmel, 2001). This data reveals that numerous outburst floods have occurred during

the glaciers rapid retreat since 1974 (Figure 25). However, prior to 1976 it is unknown whether lake levels remained constant or had periodic outburst (Krimmel, 2001). The deposit in question represents the only gravity flow deposit, except for the 1964 Earthquake deposit, recorded for the upper 120cm (100 years) of the core. Therefore, if glacial outburst floods had occurred at the same frequency prior to 1976, it is likely that a greater number of gravity flow deposits would be observed at depths greater than the deposit in question.

In addition to a lack of gravity flow deposits prior to 1976, there are no additional gravity flow deposits, except for the deposit in question, corresponding to the large number of outbursts recorded since 1976. The scarcity of gravity flow deposits may be a result of the Glaciers rapid retreat behind a shoal during the early 1980's. From 1974-1983 a western portion of the Glacier terminated on a 30m deep shoal (Meier et al., 1985). However, in 1984 the Glacier terminated ~2,000m behind the crest of the shoal in 300m of water. The presence of this shoal since 1984 may have prevented any gravity flows emanating from the Columbia Glacier from traveling further downslope. Furthermore it should be noted that since 2000, the glacier has retreated past both Lake Kadin and Lake Terentiev and these lakes are no longer dammed by ice and capable of producing outburst floods.

While an outburst flood from the Columbia Glacier could have occurred within the time period of the gravity flow deposit in question; no data exists on the sediment concentrations within these outburst flows, and there have been no recorded observations of plunging hypopycnal flows. Furthermore, outburst flood deposits retrieved from the Bearing Glacier, located to the east of the Copper River, showed no signs of gravity

driven transport despite thick flood deposits and steep seabed gradients (Jaeger and Nittrouer, 1999). Therefore the more reasonable conclusion is that the upper gravity flow deposit in core P-12 was triggered by an earthquake and represents an analogue to the 1964 gravity flow deposit.

Historic earthquake data reveal that two earthquakes occurred near the Columbia Glacier in 1983; a surface wave magnitude (M_s) 6.4 earthquake that occurred ~30km to the west of the Glacier on June 12th, and a M_s 6.3 earthquake that occurred ~35km to the west of the Columbia Glacier on September 7th (Figure 22) (USGS, 2014B). While both earthquakes could have potentially caused a gravity flow at coring location P-12, the June 12th earthquake represents the more likely trigger, as this earthquake occurred first and likely remobilized the unconsolidated sediment that had been accumulating on the steep slopes since 1964. Furthermore, this earthquake represents the only earthquake larger than M_s 6.0 (except for the Sept 7, 1983 earthquake) to have occurred within 200km of core P-12 from 1964 to the time of core retrieval. I hypothesize that this earthquake remobilized the fine-grained sediment that had been accumulating on the steep slopes in this region since the 1964 Earthquake, which then travelled downslope as a gravity flow to coring location P-12 before being deposited.

A corresponding deposit can be identified in core P-10 as a diffuse layer of grey-blue sediment from 24-28cm that contains a slight peak in the K/Ca ratio and dates to early 1980's based on the core's geochronology. Furthermore, the Sr/Pb ratio indicates that this blue-grey sediment is finer grained than the background sediment. Based on this evidence, I hypothesize that this deposit is the distal run out of the gravity flow that produced the 1983 deposit in core P-12.

1912 and 1890 Gravity Flows

Peaks in the K/Ca ratio also corresponded to two additional regions of core P-12 that contained grey-blue colored sediment similar to the core's 1964 and 1983 gravity flow deposits (Figure 14). The first deposit is from 120-130cm, and displays a peak in K/Ca and a corresponding decrease in grain size as shown by the Sr/Pb ratio. Based on the core's geochronology this deposit dates to the early 1910's. While a glacial outburst flow cannot be entirely ruled out as the cause of these deposits, historic earthquake records for the region were used to identify possible seismic triggers.

Earthquake records revealed that two earthquakes greater than magnitude 6.0 occurred within 100km of the Columbia Glacier between 1900 and 1964; a body wave magnitude (m_b) 7.0 located 30km to the west of the Glacier on January 31, 1912, and a M_s 6.8 located ~100km to the south of the Columbia Glacier on July 6, 1928 (Figure 22) (USGS, 2014B). Based on the cores geochronology it is likely that this deposit was from the 1912 earthquake; as this earthquake was larger and closer. The absence of a 1928 deposit may be due to the greater distance from the earthquake epicenter to the glacier. Alternatively, easily remobilized sediment may not have been replenished on the channel slopes since the 1912 event.

The deepest K/Ca peak in core P-12 was centered around 145cm where core photographs revealed similar grey-blue colored sediment and a decrease in grain size (Sr/Pb) that was characteristic of the other gravity flow deposits. The ^{210}Pb geochronology model for core P-12 does not extend to the region of the core where this deposit was observed, as supported ^{210}Pb values were reached at 120cm, however using the sedimentation rate for the upper portion of the core this deposit can be estimated to

have occurred in the early 1890's. Reliable historic earthquake data is not available prior to 1900, however based on the properties of the deposit it is likely that an earthquake, or outburst flood, occurred in the Columbia Glacier region in the early 1890's that caused a southward propagating gravity flow.

The lack of corresponding 1910's and 1890's gravity flow deposits in core P-10 (Figure 15) may be due to the strength of the flow or a change in the central channel bathymetry which may have blocked the pathway of the flows from reaching coring location P-10. Alternatively, if the northerly gravity flows were able to deposit sediment at coring location P-10, the deposit may not have been thick enough to be preserved and detected, as surface mixing of gravity flow sediment with background sediment may have diluted the physical and geochemical signature of a gravity flow composed of Columbia Glacier sediment.

Seasonal Sediment Deposits

High sedimentation rates, the absence of significant bioturbation, and a close proximity to Hinchinbrook Entrance makes cores P-7 and P-8 ideal to test the potential for XRF elemental ratios to be used as proxies for seasonal sedimentation. The intense physical layering in core P-7 appears to reflect seasonal sediment sources, whereas the redox banding in core P-8 appears to be the result of seasonal variations in the concentration and or composition of organic matter preserved in the sediment.

Grain Size – Sr/Pb

The inter-bedded coarse and fine-grained layers of core P-7 can be tracked using the XRF Sr/Pb ratio. Furthermore, due to the XRF core scanners 5mm spatial resolution, the Sr/Pb ratio generates near continuous down-core grain size profiles. For example, the Sr/Pb ratio tracks even the fine-scale (<5mm) laminations in the x-radiograph of core P-7 (Figure 16).

The Sr/Pb profile of core P-7 displayed a cyclic pattern that was most pronounced from 89-128cm (Figure 26). For this region of the core, the visually interpreted wavelength of the Sr/Pb cyclicity ranged from 4.0 - 5.5cm and had an average value of 4.8cm. Furthermore, a Fast Fourier Transform (FFT) analysis of the Sr/Pb values from 96-128cm revealed that the dominant period (wavelength) was 4.6cm. The similarities between this dominant wavelength and the core averaged sedimentation of $4.4\text{cm}\text{yr}^{-1}$ suggest that a Sr/Pb wavelength represents an annual sediment deposit. The cyclic nature of grain size within these annual deposits is interpreted to be the result of variations in sediment source.

The coarse-grained layers in core P-7 are interpreted to be the result of the coarse-grained sediment transported from the nearshore region to the East of Hinchinbrook Entrance during the winter season. Winter storms that form in the Gulf of Alaska, in response to the development of the seasonal AL, are capable of producing waves with bottom orbital velocities great enough to resuspend sediment to depths greater than 60m (Jaeger and Nittrouer, 2006). Additionally, increased southeasterly wind speeds associated with the formation of the AL increase the speed and therefore erodibility and transport capacity of the ACC. It is believed that this seasonal increase in both wave and

current energy is the most likely explanation for the seasonal deposition of coarse-grained sediments.

Fine-grained sediment is also likely resuspended by waves and currents during the winter season, however due to lower shear stresses needed for transport and slower settling velocities, these finer sediments are likely advected further northward into the Sound, beyond coring location P-7, before being deposited. Additionally, during the winter months the discharge of the Copper River is minimal; therefore fine-grained sediments from the Copper River are not being directly deposited at Hinchinbrook Entrance from the Copper River plume during this time period.

In contrast to the coarse layers, the interbedded fine-grained layers observed in core P-7 are interpreted to be the result of fine-grained sediments from the Copper River plume being deposited in Hinchinbrook Entrance during the summer season. During this time period average wind and wave conditions in the Gulf of Alaska are much calmer than the winter months, therefore the transport of nearshore coarse-grained sediment would be significantly less. Additionally, during the summer months the discharge of sediment from the Copper River is at its annual maximum. The presence of thin coarse layers within a larger fine-grained summer “seasonal layer” are likely due high wind and wave events that episodically occur during the summer season.

While the conceptual model described above appears to fit well for the region of the core from 89-128cm, there is an absence of the pronounced “seasonal layers” from 60-89cm. The x-radiograph for this region of the core reveal small scale laminations that are difficult to visually separate into seasonal signals based on the Sr/Pb ratio. The FFT for this region revealed a dominant wavelength of 8cm. Visually dividing this region into

~8cm wavelength, it is apparent that wavelength contains many coarse and fine-grained laminations. This region may represent a period of time when the transport of coarse-grained sediments occurred in both the summer and winter months. Alternatively, the absence of thick fine-grained intervals may be due a decrease in the amount of Copper River sediment deposited during the summer months; which may be due to a temporary change in the flow of the ACC.

From 18-60cm there also appears to be strong Sr/Pb cyclicity, similar to that from 90-128cm. The visually interpreted wavelength for the core section was on average 4.7cm. However, the FFT for this region shows a dominant wavelength of 6.5cm with minor wavelengths of 5.3cm and 4cm. The cause of the discrepancy between a 6.5cm dominant wavelength and those wavelengths picked visually may be due to the presence of multiple Sr/Pb peaks within a coarse layer. Additionally, annual variations in the sedimentation rate may reduce the ability for the FFT to identify a dominant annual wavelength that is agreement with the core average sedimentation rate.

From 0-18cm the core does not display interbedded coarse- and fine-grained layers in the photograph or x-radiograph, however the Sr/Pb ratio does display some cyclic variations. The uniform appearance of the topmost section of the core P-7 is thought to be due to accidental sediment homogenization during the core retrieval process.

In summary, the Sr/Pb ratio was a useful proxy to look at seasonal sedimentation trends in the southern region of Hinchinbrook Entrance. Additionally there is a high potential for the Sr/Pb ratio to be used as a proxy for resuspension in the Gulf of Alaska;

which itself may be related to regional climatic drivers such as the Arctic Oscillation and Pacific Decadal Oscillation that influence the strength and position of the AL.

Marine Organic Matter – Br/Cl

The smoothed (3-point running average) Br/Cl profile for the lower region of core P-8 generally showed higher values corresponding to the dark colored redox bands and lower values corresponding to the interbedded light colored redox bands (Figure 20). The relatively uniform thicknesses of these redox bands resulted in cyclic variations in the Br/Cl ratio. This cyclicity may be the result of seasonal variations in primary productivity. During the spring through fall months, primary productivity in the coastal waters is high, whereas during the winter months primary productivity is low (Eslinger et al., 2001). Therefore, the combination of a seasonal dark and light redox band may represent an annual deposit. The thickness of the annual deposits in the lower half of Core P-9, as determined by visual interpretation, range from 3.0 – 8.0cm and had an average thickness of 5.0cm (Figure 27). This average “annual deposit” thickness is not unrealistic given the core averaged ^{210}Pb sedimentation rate of 4.0cm yr^{-1} .

While primary productivity and the flux of marine organic matter to the sediments may be seasonal; the Br/Cl ratio of the corresponding sediment deposits may be influenced by grain size. Grain size determines the total surface area of the sediments which determines how much organic matter may be adsorbed; i.e. finer grained sediments have a higher surface areas and higher concentrations of adsorbed organic matter (e.g., Tanoue and Handa, 1979; Mayer, 1994; Ransom et al., 1998). Therefore, the use of the Br/Cl ratio as a proxy for seasonal sedimentation is most reliable when grain size

variations are not observed, or during ideal seasonal conditions; i.e. fine-grained sediments deposited in summer, coarse-grained sediments deposited in the winter. For example, ideal seasonal conditions appear to have occurred from 126-130cm. In this interval the two black redox bands (summer deposits) have low Sr/Pb values and high Br/Cl values.

However, during non-ideal conditions coarse-grained sediments may be deposited during the summer complicating the reliability of Br/Cl ratio as a proxy for seasonal deposition. For example, the dark redox band centered at 100cm would be expected to have a high Br/Cl ratio compared to the adjacent light redox bands based on the proposed model. However, because grain size (Sr/Pb) was greater in the dark redox band compared to the adjacent light redox bands, the corresponding Br/Cl ratio was lower than expected. Furthermore, a decrease in grain size (Sr/Pb) at 97.5cm likely caused the corresponding Br/Cl peak in the light colored redox band.

Interestingly, specific redox bands, such as the one centered at 100cm, appeared to be independent of the Br/Cl (marine organic matter) yet still showed cyclic variations based on color; which are assumed to be caused by redox gradients caused by seasonal variations in organic matter deposition. One explanation for this offset is that the redox bands are not entirely caused by seasonal variations in primary production, but are in part due to seasonal variations in the flux of terrestrial organic matter through river discharge. Alternatively, seasonal redox conditions may be caused by variations in dissolved oxygen concentrations, which may be in part driven by seasonal variations in the upwelling and downwelling. For example, intense downwelling conditions are experienced throughout the winter months, due to increased southeasterly winds, and as a result bottom waters

likely contain relatively high dissolved oxygen levels. In comparison, during the summer months wind speeds relax and upwelling conditions may form, which allows for bottom water from along the shelf to enter the Sound (Figure 5) (Niebauer et al., 1994; Jaeger and Nittrouer, 2006). This upwelled water may contain relatively low dissolved oxygen concentrations, which may lead to lower aerobic decomposition of organic matter at the surface of the seabed and therefore higher concentrations of buried organic matter.

Higher concentrations of organic matter at depth may result in reducing conditions and the formation of iron sulfides responsible for the observed redox banding. However, without further organic matter analysis on the retrieved sediment cores (e.g., total organic carbon; C:N ratios; $\delta^{13}\text{C}$), and an analysis seasonal dissolved oxygen levels within bottom waters of the Sound, it cannot be known what exactly is responsible for the cyclic redox banding observed in core P-8.

In summary, the Br/Cl ratio must be interpreted with caution as down core variations in water content and grain size complicate its reliability as a proxy for seasonal primary production and sediment deposition. The Br/Cl proxy may prove useful for regions of PWS where sedimentation rates are high enough to preserve the sedimentary fabric, but where down core grain size remains uniform. These two conditions were not observed in any of the PWS cores collected for this study, however they may potentially be occurring between cores P-8 and P-9; as core P-8 was too far south and therefore received seasonal inputs of coarse-grained sediment while core P-9 was too far north and therefore did not have a high enough sedimentation rate to preserve seasonal layers.

CONCLUSIONS

- 1) There are two major sediment sources to the central channel region of PWS; an allochthonous source of sediment that is advected into PWS through Hinchinbrook Entrance, and an autochthonous source of sediment from northern PWS. The allochthonous source of sediment likely represents a combination of sediment transported directly from the Copper River as part of the suspended sediment plume and resuspended sediment from the nearshore region that likely has multiple sources, whereas the autochthonous source of sediment likely comes from the Columbia Glacier region of northern PWS.

- 2) In the northern portion of PWS, sediment is episodically transported downslope from the Columbia Glacier region as earthquake initiated gravity flows that can be geochemically identified based on their color, grain size, and XRF K/Ca signature.

- 3) In southern Hinchinbrook Entrance, seasonal sedimentation is preserved as variations in grain size that are interpreted to be the result of seasonal wave and current conditions along the Gulf of Alaska that are driven by the formation of the Aleutian Low in the winter and North Pacific High in the summer. In the proposed model, coarse-grained sediments are deposited during energetic winter conditions while fine-grained sediments are deposited during moderate summer conditions. These seasonal deposits can be identified based on the cyclicity of the XRF Sr/Pb ratio.

4) In northern Hinchinbrook Entrance, uniform redox banding, observed as ephemeral light and dark colored laminations, was likely caused by multiple factors including seasonal variations in primary production, the flux of terrestrial organic matter through river discharge, grain size, and the dissolved oxygen concentration of bottom waters driven by upwelling-downwelling conditions. A general correlation between the XRF Br/Cl ratio and the redox banding suggests that at least portion of the organic matter within these bands is of marine origin. However, the use of the Br/Cl as a proxy for seasonal sedimentation should be used with caution due to complicating relationships with grain size and water content.

5) Distinct seasonal sediment deposits are in part due to the effects of the seasonal formation of the Aleutian Low (i.e. wind, waves, currents, and upwelling), which is in turn influenced by climatic drivers such as the Pacific Decadal and Arctic Oscillation. Therefore, with longer sediment cores it may be possible to create paleo-climatic records for the PWS region.

LITERATURE CITED

- Addison, J., Finney, B., Jaeger, J., Stoner, J., Norris, R., Hangsterfer, A., 2013. Integrating satellite observations and modern climate measurements with the recent sedimentary record: An example from Southeast Alaska. *Journal of Geophysical Research: Oceans* 118, 3444-3461.
- Alaska Earthquake Information Center (AEIC), 2006. Alaska Earthquake Facts. Retrieved from: <http://www.aeic.alaska.edu>
- Alyeska Pipeline, 2014. Pipeline Facts. Retrieved online from: <http://www.alyeska-pipe.com>
- Borovec, Z., 2000. Elements in size-fractionated bottom sediments of the Elbe River in its Czech part. *Aquatic Sciences* 62, 232-251.
- Brabets, T., 1996. Geomorphology of the lower Copper River, Alaska. United States Geological Survey Professional Paper 1581.
- Brown, E., Johnson, T., Scholz, C., Cohen, A., King, J., 2007. Abrupt change in tropical African climate linked to the bipolar seesaw over the past 55,000 years. *Geophysical Research Letters* 34. doi: 10.1029/2007GL031240.
- Carlson, P., Bruns, T., Molnia, B., Schwab, W., 1982. Submarine valleys in the northeastern Gulf of Alaska: Characteristics and probable origin. *Marine Geology* 47, 217-242.
- Carlson, P., Molnia, B., 1978. Minisparker profiles and sedimentologic data from the R/V "Acona" cruise (April 1976) in the Gulf of Alaska and Prince William Sound. United States Geological Survey Open-File Report 78-381.
- Carlson, P., Molnia, B., Kittleson, S., Hampson, J., 1977. Distribution of bottom sediments on the continental shelf, northern Gulf of Alaska, Scale 1:500,000. United States Geological Survey Miscellaneous Field Study Map MF-876, 1-13.
- Carlson, P., Molnia, B., Quintero, P., 1978. Transport of inner shelf sediment into glacially scoured trough, northeastern Gulf of Alaska. *Trans. Am. Geophys. Union, EOS*, 59, P. 1109 (Abstract).
- Cauwet, G., 1987. Influence of sedimentological features on the distribution of trace metals in marine sediments. *Marine Chemistry* 22, 221-234.
- Cutshall, N., Larsen, I., Olsen, C., 1983. Direct analysis of ^{210}Pb in sediment samples: Self-absorption corrections. *Nuclear Instruments and Methods* 206, 309-312.

- Cuven, S., Francus, P., Lamoureux S., 2010. Estimation of grain size variability with micro X-ray fluorescence in laminated lacustrine sediments, Cape Bounty, Canadian High Arctic. *Journal of Paleolimnology* 44, 803-817.
- Eslinger, D., Cooney, R., McRoy C., Ward, A., Kline, T., Simpson, E., Wang, J., Allen, J., 2001. Plankton dynamics: observed and modelled responses to physical conditions in Prince William Sound, Alaska. *Fisheries Oceanography* 10, 81-96.
- Feely, R., Baker, E., Schumacher, J., Massoth, G., Landing, W., 1979. Processes affecting the distribution and transport of suspended matter in the northeast Gulf of Alaska. *Deep-Sea Research* 26A, 445-464.
- Gracia, E., Vizcaino, A., Escutia, C., Asioli, A., Rodes, A., Pallas, R., Garcia-Orellana, J., Lebreiro, S., Goldfinger, C., 2010. Holocene earthquake record offshore Portugal (SW Iberia); testing turbidite paleoseismology in a slow-convergence margin. *Quaternary Science Reviews* 29, 1156-1172.
- Halverson, M., Belanger, C., Gay, S., 2013. Seasonal transport variations in the straits connecting Prince William Sound to the Gulf of Alaska. *Continental Shelf Research* 63, S63-S78.
- Hartmann, B., Wendler, G., 2005. The significance of the 1976 Pacific climate shift in the climatology of Alaska. *Journal of Climate* 18, 4824-4838.
- Hennekam, R., de Lange, G., 2012. X-ray fluorescence core scanning of wet marine sediments: methods to improve quality and reproducibility of high-resolution paleoenvironmental records. *Limnology and Oceanography: Methods* 10, 991-1003.
- Horowitz, A., Elrick, K., 1987. The relation of stream sediment surface area, grain size and composition to trace element chemistry. *Applied Geochemistry* 2, 437-451.
- Jaeger, J., Nittrouer, C., 1999. Marine record of surge-induced outburst floods from the Bering Glacier, Alaska. *Geology* 27, 847-850.
- Jaeger, J., Nittrouer, C., 2006. A quantitative examination of modern sedimentary lithofacies formation on the glacially influenced Gulf of Alaska continental shelf. *Continental Shelf Research* 26, 2178-2204.
- Jaeger, J., Nittrouer, C., Scott, N., Milliman, J., 1998. Sediment accumulation along a glacially impacted mountainous coastline; north-east Gulf of Alaska. *Basin Research* 10, 155-173.

- Jansen, J., Van der Gaast, S., Koster, B., Vaars, A., 1998. CORTEX, a shipboard XRF-scanner for element analyses in split sediment cores. *Marine Geology* 151, 143-153.
- Johnson, W., Royer, T., Luick, J., 1988. On the seasonal variability of the Alaska Coastal Current. *Journal of Geophysical Research* 93, 12,423-12,437.
- Klein, H., 1983. Provenances, depositional rates and heavy metal chemistry of sediments, Prince William Sound, southcentral Alaska. Ph.D Dissertation, University of Alaska, Fairbanks.
- Koide, M., Soutar, A., Goldberg, E., 1972. Marine Geochronology with ²¹⁰Pb. *Earth and Planetary Science Letters* 14, 442-446.
- Krimmel, R., 2001. Photogrammetric data set, 1957-2000, and bathymetric measurements for Columbia Glacier, Alaska. United States Geological Survey Water-Resources Investigations Report 01-4089.
- Krishnaswamy, S., Lal, D., Martin, J., Meybeck, M., 1971. Geochronology of lake sediments. *Earth and Planetary Science Letters* 11, 407-414.
- Kujau, A., Nurnberg, D., Zielhofer, C., Bahr, A., Rohl, U., 2010. Mississippi River discharge over the last ~560,000 years – Indications from X-ray fluorescence core scanning. *Paleogeography, Paleoclimatology, Paleoecology* 298, 311-318.
- Kylander, M., Ampel, L., Wohlfarth, B., Veres, D., 2011. High-resolution X-ray fluorescence core scanning analysis of Les Echets (France) sedimentary sequence: new insights from chemical proxies. *Journal of Quaternary Science* 26, 109-117.
- Lethcoe, J., 1990. An observer's guide to the geology of Prince William Sound, Alaska. Prince William Sound Books, Valdez.
- L'Heureux, M., Mann, M., Cook, B., Gleason, B., Vose, R., 2004. Atmospheric circulation influences on seasonal precipitation patterns in Alaska during the latter 20th century. *Journal of Geophysical Research* 109, doi:10.1029/2003JD003845
- Mayer, L., 1994. Surface area control of organic carbon accumulation in continental shelf sediments. *Geochimica et Cosmochimica Acta* 58, 1271-1284.
- Mayer, L., Schick, L., Allison, M., Ruttenger, K., Bentley, S., 2007. Marine vs. terrigenous matter in Louisiana coastal sediments: The uses of bromine:organic carbon ratios. *Marine Chemistry* 107, 244-254.
- Meier, M., Rasmussen, L., Miller, D., 1985. Columbia Glacier in 1984: Disintegration Underway. United States Geological Survey Open File Report 85-81.

- Milliman, J., Farnsworth, K., 2011. River Discharge to the Coastal Ocean: A Global Synthesis. Cambridge University Press, New York.
- Milliman, J., Stocks, D., Jaeger, J., Nittrouer, C., 1996. Prince William Sound, Alaska: distal depocenter for Copper River sediment. *EOS Transactions* 77, OS202.
- Milliman, J., Syvitski, J., 1992. Geomorphic/tectonic control of sediment discharge to the ocean: The importance of small mountainous rivers. *The Journal of Geology* 100, 525-544.
- Molnia, B., Hein, J., 1982. Clay mineralogy of a glacially dominated, subarctic continental shelf: Northeastern Gulf of Alaska. *Journal of Sedimentary Petrology* 52, 0515-0527.
- Morris, A., Riley, J., 1966. The bromide/chlorinity and sulphate/chlorinity ratio in sea water. *Deep Sea Research* 13, 699-705.
- Mulder, T., Syvitski, J., Migeon, S., Faugeres, J., Savoye B., 2003. Marine hyperpycnal flows: initiation, behavior and related deposits. A review. *Marine Geology and Petroleum Geology* 20, 861-882.
- Naidu, A., Freitag, G., Mowatt, T., 1976. Clay minerals and recent sediments of the continental shelf, northern and western Gulf of Alaska. In *Proceedings, Alaska Science Conference, 27th: Fairbanks, Alaska, v. II, Alaska Division of American Association for the Advancement of Science, University of Alaska*, p. 202-212.
- National Climatic Data Center (NCDC), 2014. Retrieved online from: <http://www.ncdc.noaa.gov/>
- Niebauer, H., Royer, T., Weingartner T., 1994. Circulation of Prince William Sound, Alaska. *Journal of Geophysical Research* 99, 14,113-14,126.
- Nittrouer, C., DeMaster, D., McKee, B., Cutshall, N., Larsen, I., 1983/1984. The effect of sediment mixing on Pb-210 accumulation rates for the Washington continental shelf. *Marine Geology* 54, 201-221.
- Nittrouer, C., Sternberg, R., Carpenter, R., Bennett, J., 1979. The use of Pb-210 geochronology as a sedimentological tool: Application to the Washington continental shelf. *Marine Geology* 31, 297-316.
- Overland, J., Adams, J., Bond, N., 1999. Decadal variability of the Aleutian Low and its relation to high-latitude circulation. *Journal of Climate* 12, 1542-1547.
- Plafker, G., 1965. Tectonic deformation associated with the 1964 Alaska Earthquake. *Science* 148, 1675-1687.

- Plafker, G., Mayo, L., 1965. Tectonic deformation, subaqueous slides and destructive waves associated with the Alaskan March 27, 1964 Earthquake; An interim geologic evaluation. United States Geological Survey Open-File Report 65-124.
- Ransom, B., Kim, D., Kastner, M., Wainwright, S., 1998. Organic matter preservation on continental slopes: importance of mineralogy and surface area. *Geochimica et Cosmochimica Acta* 58, 1329-1345.
- Richter, T., Van der Gaast, S., and Koster, B., Vaars, A., Gieles, R., De Stiger, H., Haas, H., Van Weering T., 2006. The Avaatech XRF Core Scanner: technical description and applications to NE Atlantic sediments. In: Rothwell, R., 2006. *New Techniques in Sediment Core Analysis*. Geological Society, London, Special Publications 267, 39-50.
- Ritchie, J., McHenry, J., 1990. Application of radioactive fallout Cesium-137 for measuring soil erosion and sediment accumulation rates and patterns: a review. *Journal of Environmental Quality* 19, 215-233.
- Robbins, J., Edgington, D., 1975. Determination of recent sedimentation rates in Lake Michigan using Pb-210 and Cs-137. *Geochimica et Cosmochimica Acta* 39, 285-304.
- Rodionov, S., Overland, J., Bond, N., 2005. The Aleutian Low and winter climatic conditions in the Bearing Sea. Part 1: Classification. *Journal of Climate* 18, 160-177.
- Rothwell, R., Hoogakker, B., Thomson, J., Croudace, I., Frenz, M., 2006. Turbidite emplacement on the southern Balearic Abyssal Plain (western Mediterranean Sea) during Marine Isotope Stages 1-3: An application of ITRAX XRF scanning of sediment cores to lithostratigraphic analysis. In: Rothwell, R., 2006. *New Techniques in Sediment Core Analysis*. Geological Society, London, Special Publications 267, 79-98.
- Royer, T., 1979. On the effect of precipitation and runoff on coastal circulation in the Gulf of Alaska. *Journal of Physical Oceanography* 9, 555-563.
- Royer, T., 1982. Coastal fresh water discharge in the northeast Pacific. *Journal of Geophysical Research* 87, 2017-2021.
- Royer, T., 1983. Observations of the Alaska Coastal Current. In: *Coastal Oceanography* (Ed. By H. Grade, A. Edwards and H. Svendsen) Plenum Press, New York.
- Royer, T., Vermersch, J., Weingartner, T., Niebauer, H., Muench, R., 1990. Ocean circulation influencing the Exxon Valdez Oil Spill. *Oceanography* 3, 3-10.

- Stabeno, P., Bond, N., Kachel, N., Salo, S., Schumacher, J., 2001. On the temporal variability of the physical environment over the south-eastern Bering Sea. *Fisheries Oceanography* 10, 81-98.
- Stabeno, P., Reed, R., Napp, J., 2002. Transport Through Unimak Pass, Alaska. *Deep-Sea Research II* 49, 5919-5930.
- Tanoue, E., Handa, N., 1979. Differential sorption of organic matter by various sized sediment sediments in recent sediment from the Bering Sea. *Journal of the Oceanographical Society of Japan* 35, 199-208.
- Thomson, J., Croudace, I., Rothwell, R., 2006. A geochemical application of the ITRAX scanner to a sediment core containing eastern Mediterranean sapropel units. In: Rothwell, R., 2006. *New Techniques in Sediment Core Analysis*. Geological Society, London, Special Publications 267, 65-77.
- Thorne, L., Nickless, G., 1981. The relation between heavy metals and particle size fractions within the Severn Estuary (U.K.) inter-tidal sediments. *The Science of the Total Environment* 19, 207-213.
- Tjallingii R., Rohl, U., 2007. Influence of the water content on X-ray fluorescence core scanning measurements in soft marine sediments. *Geochemistry, Geophysics, Geosystems* 8, doi:10.1029/2006GC001393.
- United States Census, 2014. Retrieved online from: <http://www.census.gov/>
- United States Geological Survey (USGS), 2013. National Geochemical Survey Database. Retrieved online from: <http://tin.er.usgs.gov/geochem>
- USGS, 2014A. The 1964 Great Alaska Earthquake & Tsunami. Retrieved online from: http://www.usgs.gov/blogs/features/usgs-_top_story/the-1964-great-alaska-earthquake-tsunami/
- USGS, 2014B. Earthquakes. Retrieved online from: <http://earthquake.usgs.gov/earthquakes/>
- Verma, H., 2007. Atomic and nuclear analytical methods: XRF, Mossbauer, XPS, NAA and ion-beam spectroscopic techniques. Springer Berlin Heidelberg, New York, 1-90.
- Whitney, P., 1975. Relationship of manganese-iron oxides and associated heavy metals to grain size in stream sediments. *Journal of Geochemical Exploration* 4, 251-263.

- Winkler, G., 2000. A geological guide to Wrangell-Saint Elias National Park and Preserve, Alaska: a tectonic collage of northbound terranes. United States Geological Survey Professional Paper 1616.
- Winkler, G., Plafker, G., 1993. Geological map of the Cordova and Middleton Island Quadrangles, southern Alaska. United States Geological Survey Miscellaneous Investigations Series Map I-1984.
- Wu, X., 2011. Transport through Prince William Sound: Numerical study in a nowcast/forecast system. *Ocean Dynamics* 61, 449-462.
- Zhang, C., Wang, L., Li, G., Dong, S., Yang, J., Wang, X., 2002. Grain size effect on multi-element concentrations in sediments from the intertidal flats of Bohai Bay, China. *Applied Geochemistry* 17, 59-68.
- Ziegler, M., Jilber, T., de Lange, G., Lourens, L., Reichert, G., 2008. Bromine counts from XRF scanning as an estimate of the marine organic carbon content of sediment cores. *Geochemistry, Geophysics, Geophysics* 9, doi: 10.1029/2007GC001932.

Table 1. Locations and depths of PWS gravity cores. Locations determined using the NAD83 GPS coordinate system. Water depths determined by shipboard depth sounder at the time of retrieval.

Core	Latitude	Longitude	Water Depth (m)
P-1	60.6014500	-145.8631667	148
P-2	60.6062500	-145.9301000	188
P-3	60.5676667	-146.4095667	123
P-5	60.3212833	-146.6226833	85
P-6	60.3155000	-146.6457167	81
P-7	60.3026000	-146.7563500	218
P-8	60.3783667	-146.7920333	290
P-9	60.4369167	-146.8104167	350
P-10	60.5030833	-146.9674667	419
P-12	60.6780000	-146.9029667	437
P-13	60.5675333	-146.5525333	136

Table 2. Core averaged percentages of sand, silt, clay, D50 (median) grain size (μm) and mean grain size (μm) with associated standard error (SE) values.

Core	% Sand	± SE	%Silt	± SE	%Clay	± SE	D50	± SE	Mean(μm)	± SE
P-1	22.1	0.9	52.1	0.4	25.9	0.6	11.8	0.6	43.7	1.1
P-2	4.3	0.1	58.7	0.2	37.0	0.2	6.1	0.1	24.2	1.2
P-3	11.8	0.6	62.0	0.5	26.2	0.3	12.1	0.3	32.0	0.9
P-5	4.8	0.3	63.2	0.3	32.0	0.4	8.0	0.2	25.9	1.6
P-6	5.8	0.2	63.8	0.3	30.4	0.3	8.7	0.2	19.7	0.7
P-7	20.5	0.9	56.4	0.7	23.1	0.5	16.6	0.9	43.9	1.2
P-8	16.2	1.1	59.1	0.6	24.8	0.7	14.8	1.0	38.9	1.6
P-9	5.6	0.8	63.7	0.4	30.8	0.6	9.1	0.7	20.0	1.3
P-10	4.4	0.4	58.5	0.3	37.0	0.5	6.4	0.1	22.6	2.1
P-12	1.1	0.3	60.7	0.8	38.3	0.8	6.2	0.3	13.0	2.7
P-13	2.5	0.3	61.2	0.6	36.3	0.7	6.7	0.4	18.5	1.8

Table 3. Sedimentation rates (cm yr^{-1}) derived from the decay of excess ^{210}Pb with depth; the depth of peak ^{137}Cs activity; and the depth of first ^{137}Cs activity. Error (+,-) for ^{210}Pb sedimentation rates represents the standard error associated with the best fit regression through excess ^{210}Pb activities with depth. The ^{210}Pb R^2 value is associated with the ^{210}Pb regression. ^{137}Cs sedimentation rate errors represent the uncertainty in defining a depth for both peak and first ^{137}Cs due to the sampling resolution.

Core	²¹⁰ Pb				Peak ¹³⁷ Cs			First ¹³⁷ Cs		
	cmyr ⁻¹	(+)	(-)	r ²	cmyr ⁻¹	(+)	(-)	cmyr ⁻¹	(+)	(-)
P-1	0.7	0.1	0.1	0.91	1.1	0.2	0.2	1.2	0.1	0.1
P-2	0.48	0.03	0.03	0.98	0.6	0.2	0.1	0.6	0.1	0.1
P-3	0.7	0.1	0.1	0.97	-	-	-	-	-	-
P-5	1.7	0.1	0.1	0.97	1.6	0.2	0.2	1.6	0.1	0.1
P-6	2.6	0.2	0.1	0.92	2.03	0.03	0.03	2.2	0.3	0.1
P-7	4.4	0.5	0.4	0.77	>3.0	-	-	-	-	-
P-8	4.0	0.4	0.3	0.80	>3.4	-	-	-	-	-
P-9	2.1	0.2	0.2	0.86	1.7	0.7	0.7	2.0	0.1	0.1
P-10	1.1	0.1	0.1	0.89	1.0	0.1	0.1	1.0	0.1	0.1
P-12	1.33	0.05	0.04	0.98	1.2	0.1	0.1	1.4	0.1	0.1
P-13	0.34	0.03	0.03	0.96	0.4	0.1	0.1	0.7	0.1	0.1

Table 4. Core P-12 correlations between K-Ca, K-Cl and Ca-Cl for regions of the core with and without observed peaks in the K/Ca ratio. In peak K/Ca regions of the core the correlations between K-Ca and Ca-Cl were significantly different than for regions of the core without peaks in the K/Ca ratio.

Region of Core	Depth (cm)	K-Ca (r)	K-Cl (r)	Ca-Cl (r)
K/Ca peak-1	32-38	0.28	0.97	0.34
K/Ca peak-2	55-70	0.57	0.71	0.21
K/Ca peak-3	120-129	0.59	0.93	0.58
K/Ca peak-4	140-149	0.72	0.97	0.69
Non K/Ca peak areas	0-32; 38-55; 70-120; 129-140	0.96	0.87	0.81

Table 5. Core P-7 correlation table between high resolution grain size measurements (percent sand, silt, clay, mean diameter (μm)) and XRF elemental intensities. Bi intensities are not shown due to unreliable XRF results in the upper half of the core where the high resolution grain size subsamples were taken. Specifically, in the upper half of the core Bi tracked grain size in the same manner as Sr, and Bi counts were centered around 16,000. In the lower core half Bi did not track grain size in the same manner as Sr, and Bi counts were below 1,000. Furthermore, in the rest of the cores Bi did not show a correlation to grain size and Bi intensities were similar to those in the lower half of Core P-7. Therefore, Bi intensities in the upper half of Core P-7 are believed to be erroneous.

	Sand (%)	Silt (%)	Clay (%)	Mean Diameter (μm)
Al	0.24	-0.30	-0.13	0.14
Si	0.27	-0.33	-0.16	0.16
P	0.07	-0.12	0.01	0.00
S	-0.16	0.22	0.07	-0.03
Cl	-0.29	0.36	0.18	-0.19
Ar	-0.21	0.25	0.15	-0.12
K	-0.05	-0.02	0.17	-0.15
Ca	0.09	-0.14	-0.01	-0.01
Ti	-0.29	0.22	0.39	-0.37
Cr	0.38	-0.42	-0.31	0.33
Mn	-0.45	0.39	0.55	-0.50
Fe	-0.60	0.54	0.68	-0.64
Rh	0.01	0.05	-0.09	0.06
Ba	-0.16	0.13	0.21	-0.26
Ni	-0.62	0.62	0.60	-0.67
Cu	-0.82	0.78	0.86	-0.82
Zn	-0.80	0.76	0.84	-0.80
Ga	0.32	-0.31	-0.34	0.37
Br	-0.82	0.79	0.85	-0.77
Rb	-0.88	0.86	0.90	-0.84
Sr	0.91	-0.87	-0.95	0.91
Y	0.00	0.01	-0.01	0.05
Zr	0.83	-0.81	-0.85	0.80
Nb	-0.57	0.50	0.66	-0.55
Mo	-0.20	0.14	0.28	-0.33
Pb	-0.85	0.83	0.87	-0.79
Sr/Pb	0.91	-0.89	-0.93	0.88

Table 6. Core P-8 correlation table between high resolution grain size measurements (percent sand, silt, clay, mean diameter (μm) and XRF elemental intensities.

	Sand (%)	Silt (%)	Clay (%)	Mean Diameter (µm)
Al	0.72	-0.66	-0.80	0.72
Si	-0.83	0.78	0.89	-0.82
P	-0.90	0.87	0.94	-0.90
S	0.82	-0.77	-0.88	0.82
Cl	0.83	-0.78	-0.89	0.82
Ar	0.82	-0.76	-0.88	0.81
K	-0.84	0.79	0.90	-0.84
Ca	-0.77	0.72	0.84	-0.77
Ti	-0.85	0.80	0.90	-0.85
Cr	-0.64	0.64	0.63	-0.66
Mn	-0.86	0.82	0.91	-0.86
Fe	-0.90	0.86	0.94	-0.90
Rh	0.03	0.01	-0.08	0.03
Ba	-0.61	0.56	0.68	-0.66
Ni	-0.56	0.54	0.58	-0.57
Cu	-0.75	0.72	0.80	-0.77
Zn	-0.91	0.88	0.94	-0.91
Ga	-0.26	0.24	0.29	-0.24
Br	0.27	-0.19	-0.38	0.29
Rb	-0.84	0.80	0.88	-0.84
Sr	0.90	-0.91	-0.86	0.88
Y	-0.51	0.45	0.59	-0.51
Zr	0.58	-0.58	-0.58	0.56
Nb	-0.14	0.18	0.09	-0.16
Mo	-0.19	0.19	0.19	-0.13
Pb	-0.88	0.86	0.90	-0.89
Bi	-0.22	0.27	0.16	-0.27
Sr/Pb	0.94	-0.93	-0.93	0.94

Table 7. Core P-9 correlation table between high resolution grain size measurements (percent sand, silt, clay, mean diameter (μm) and XRF elemental intensities.

	Sand (%)	Silt (%)	Clay (%)	Mean Diameter (μm)
Al	-0.44	0.59	0.32	-0.38
Si	-0.19	0.47	0.07	-0.13
P	0.43	-0.09	-0.47	0.47
S	0.66	-0.55	-0.58	0.56
Cl	0.05	-0.37	0.06	-0.03
Ar	0.71	-0.10	-0.79	0.70
K	-0.92	0.42	0.92	-0.89
Ca	-0.47	0.22	0.47	-0.44
Ti	-0.93	0.40	0.94	-0.90
Cr	0.65	-0.51	-0.58	0.67
Mn	-0.95	0.37	0.97	-0.93
Fe	-0.95	0.41	0.96	-0.95
Rh	-0.78	0.11	0.86	-0.80
Ba	-0.66	0.25	0.68	-0.60
Ni	-0.54	-0.14	0.67	-0.47
Cu	-0.76	0.33	0.77	-0.82
Zn	-0.94	0.57	0.90	-0.96
Ga	-0.48	0.49	0.39	-0.58
Br	-0.26	-0.02	0.30	-0.23
Rb	-0.93	0.56	0.89	-0.91
Sr	0.86	-0.42	-0.86	0.87
Y	0.23	-0.20	-0.21	0.39
Zr	0.80	-0.60	-0.72	0.84
Nb	-0.58	-0.04	0.67	-0.53
Mo	0.76	-0.38	-0.76	0.77
Pb	-0.98	0.57	0.94	-0.97
Bi	-0.22	0.11	0.22	-0.13
Sr/Pb	0.98	-0.52	-0.96	0.97

Table 8. Core P-12 correlation table between high resolution grain size measurements (percent sand, silt, clay, mean diameter (μm) and XRF elemental intensities.

	Sand (%)	Silt (%)	Clay (%)	Mean Diameter (µm)
Al	-0.58	-0.32	0.36	-0.47
Si	-0.46	-0.09	0.14	-0.32
P	-0.45	-0.26	0.29	-0.34
S	0.52	0.33	-0.37	0.44
Cl	0.57	0.28	-0.32	0.46
Ar	0.68	0.57	-0.61	0.70
K	-0.78	-0.73	0.76	-0.77
Ca	0.23	0.31	-0.32	0.29
Ti	-0.56	-0.43	0.46	-0.53
Cr	-0.44	-0.05	0.09	-0.32
Mn	-0.47	-0.82	0.81	-0.60
Fe	-0.52	-0.83	0.82	-0.64
Rh	0.01	0.24	-0.22	0.03
Ba	-0.42	-0.35	0.37	-0.34
Ni	-0.23	-0.58	0.56	-0.38
Cu	-0.17	-0.40	0.39	-0.26
Zn	-0.62	-0.88	0.89	-0.78
Ga	-0.50	-0.49	0.51	-0.62
Br	0.17	-0.39	0.34	-0.06
Rb	-0.67	-0.86	0.87	-0.77
Sr	0.59	0.97	-0.97	0.76
Y	-0.45	-0.15	0.19	-0.26
Zr	0.16	0.49	-0.48	0.23
Nb	-0.47	-0.77	0.76	-0.59
Mo	-0.65	-0.63	0.65	-0.64
Pb	-0.64	-0.86	0.87	-0.78
Bi	0.14	-0.05	0.03	0.01
Sr/Pb	0.60	0.95	-0.95	0.79

Figure 1. Accretionary terranes of the Prince William Sound and Copper River basins (red lines). The Prince William Sound basin is composed of the Prince William Sound Terrane (light blue – PW) and Chugach Terrane (light blue - CG) which are separated by on the map by the yellow dashed line. In addition to the PW and CG terranes, the Copper River basin is also composed of the Wrangellia Composite Terrane (green). Modified from Winkler (2000).

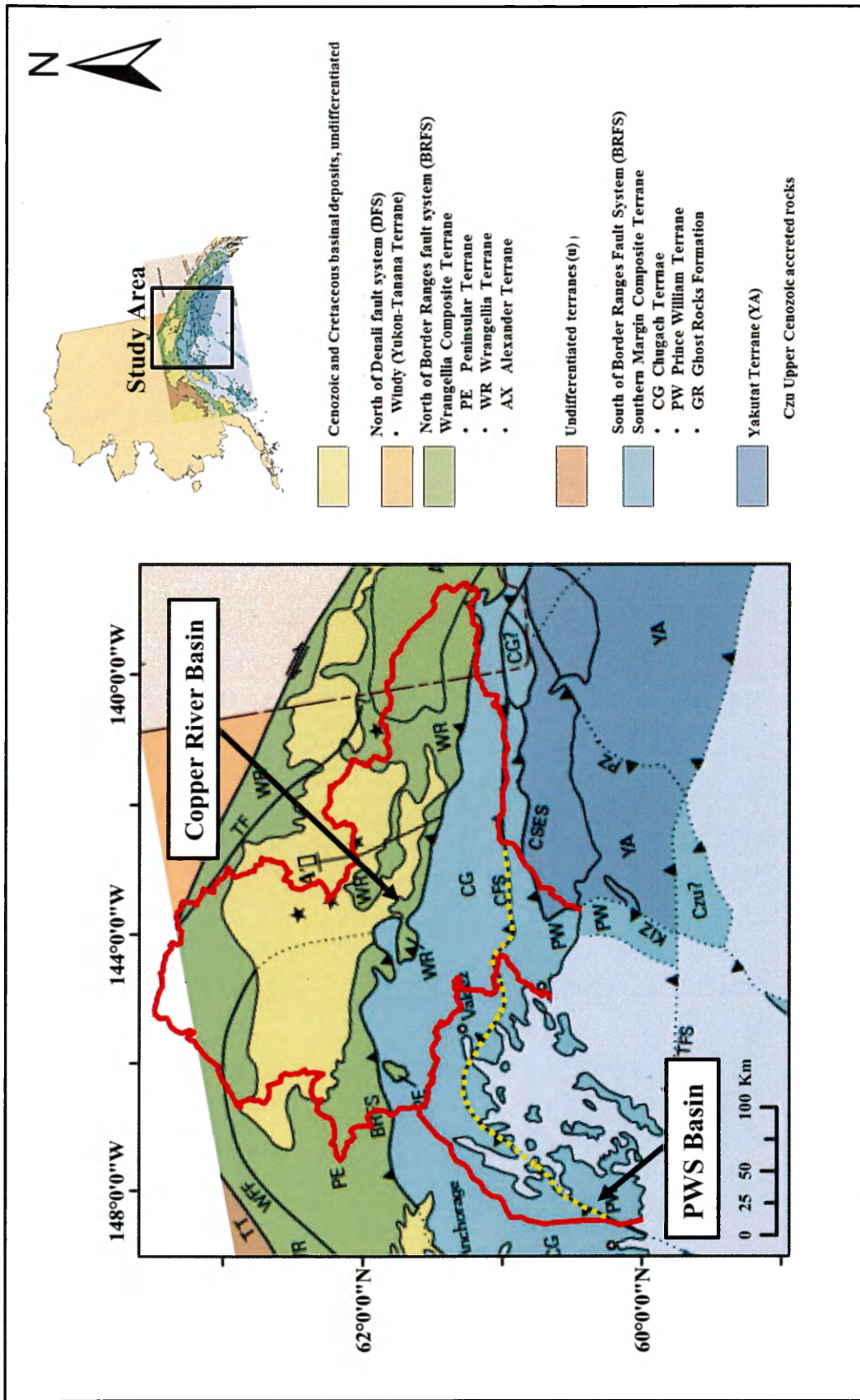


Figure 2. Surficial geology of the Prince William Sound and Copper River basins. The Prince William Sound basin contains Orca and Valdez Group metasedimentary rocks, whereas the Copper River Basin also contains igneous rocks. Data obtained from United States Geological Survey.

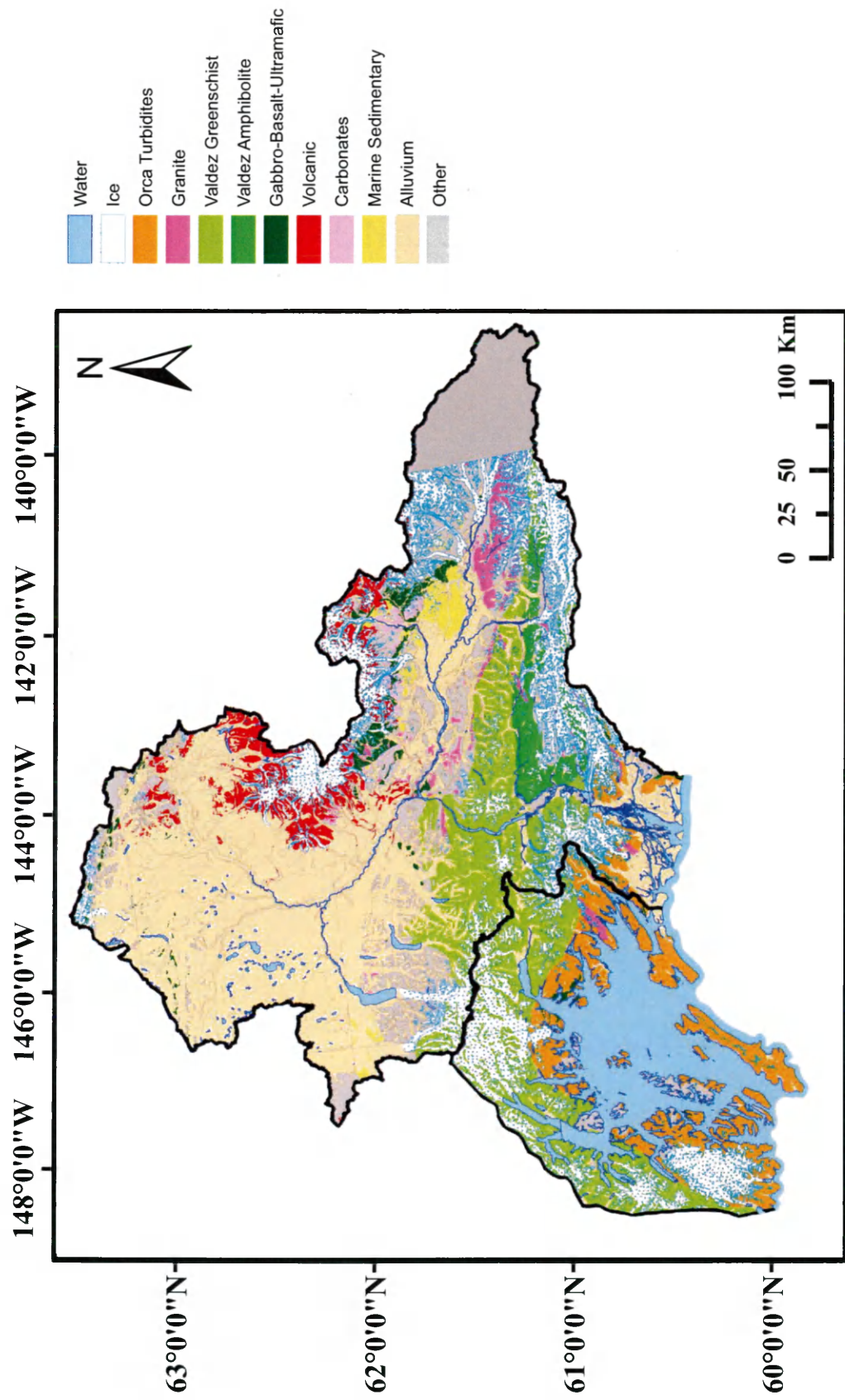


Figure 3. Bathymetry of Prince William Sound shown with a 50m contour interval.

Summer 2012 coring locations shown by red circles. See Table 1 for water GPS

coordinates and water depths for individual coring locations.

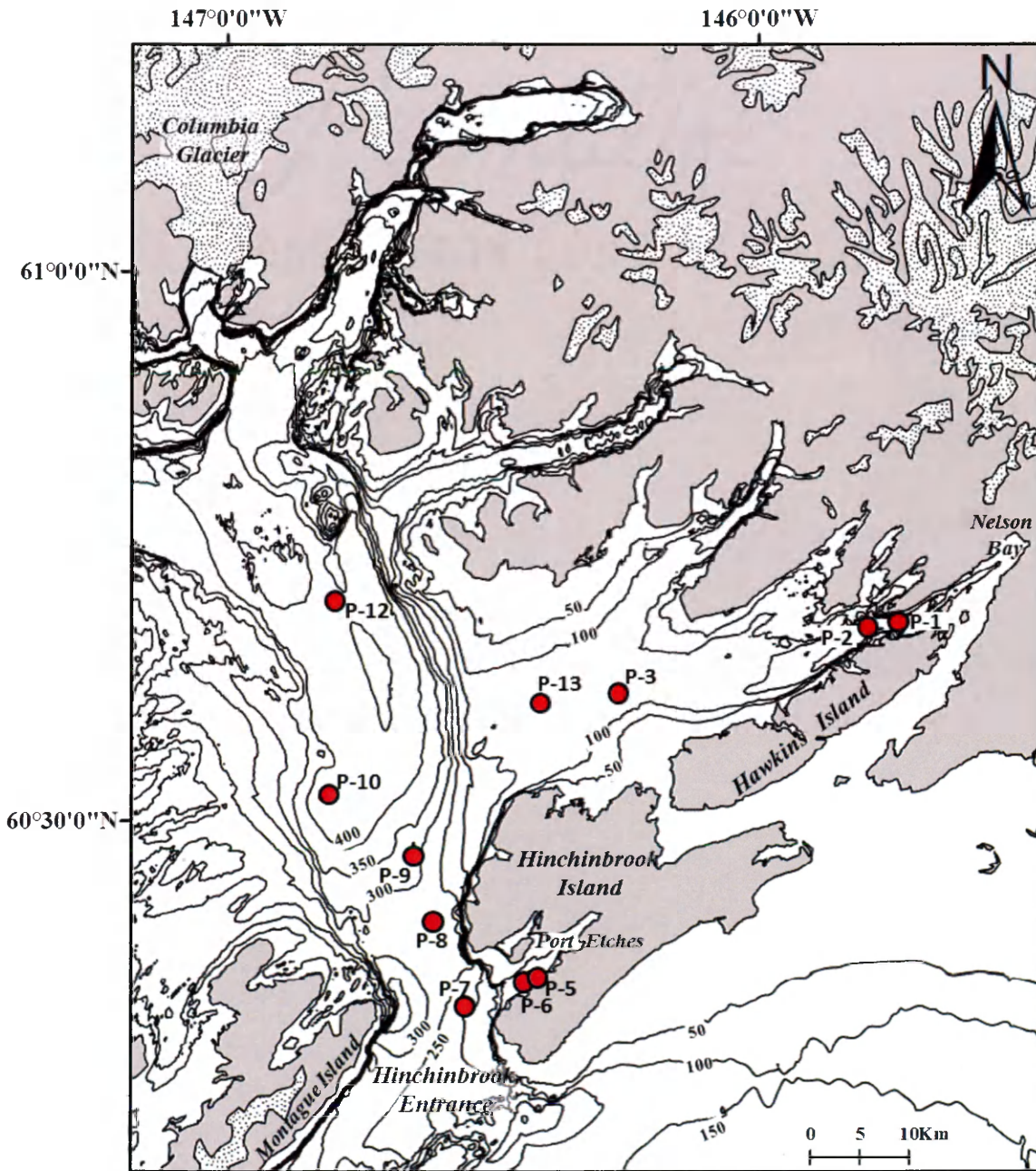


Figure 4. Conceptual pathway of the Alaska Coastal Current (dashed red line) modified after Royer et al., (1990) overlain on the August 28, 2011 MODIS satellite image. The current can be seen deflecting the Copper River sediment plume towards the west. At Hinchinbrook Entrance a portion of the current and entrained sediment bifurcates northward and enters the Sound.

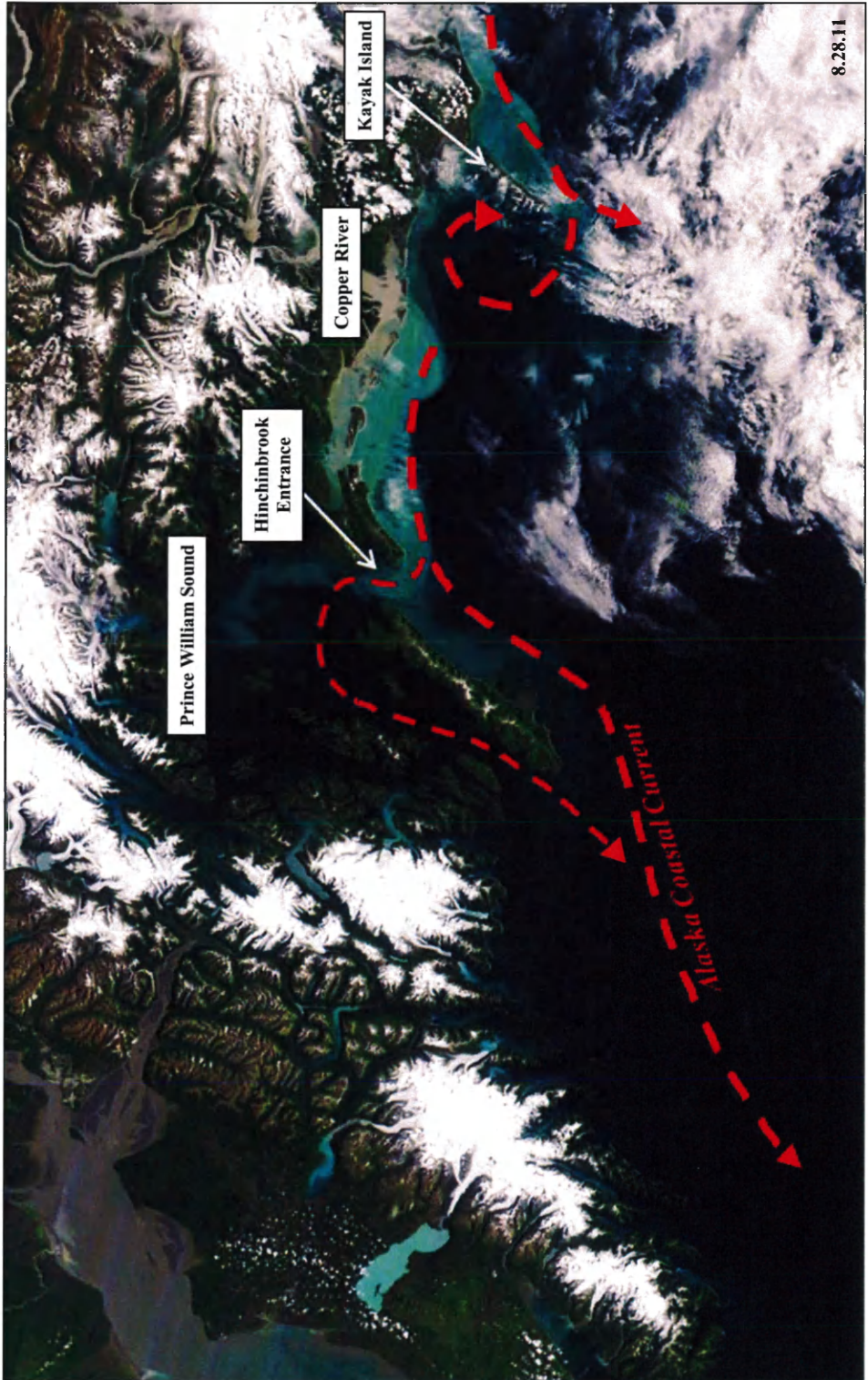


Figure 5. Seasonal variations in the average water (1958-1998) and sediment(1991-1993) discharge from the Copper River (top); the upwelling index (1946-2004) for 60°N 146°W (offshore of Prince William Sound); significant wave heights (1975-2001) from the National Oceanic and Atmospheric Administration's Buoy 46001 (near Kodiak, Alaska) (middle) and wave associated bottom orbital velocities at 40m and 60m water depths (bottom). Shaded bars represent one standard deviation; error bars represent minimum and maximum values. During the summer months river discharge is high while sea state and upwelling conditions decrease. During the winter months the reverse trend is observed. From Jaeger and Nittrouer (2006).

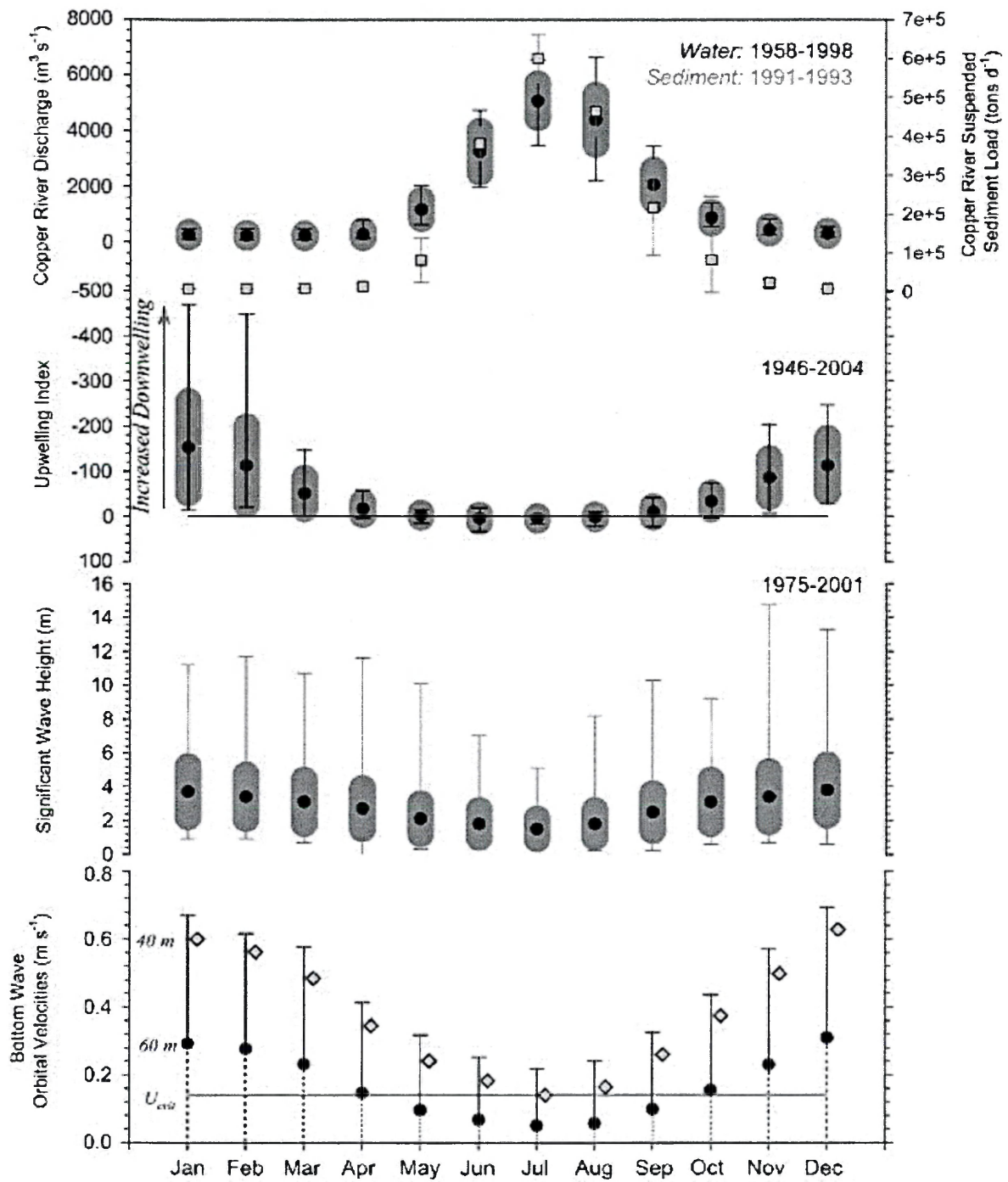


Figure 6. 2012 continuous discharge data for the Copper River at The Million Dollar Bridge (blue line) (USGS), and daily rainfall totals from nearby Cordova (orange line) (NCDC, 2014). During the spring-early summer discharge is believed to be driven by the melting of the winter snowpack. After the majority of the snowpack has melted, discharge is believed to be driven by glacial melt during the mid-late summer. Peaks in discharge during the fall are believed to be driven by high amounts of coastal rainfall.

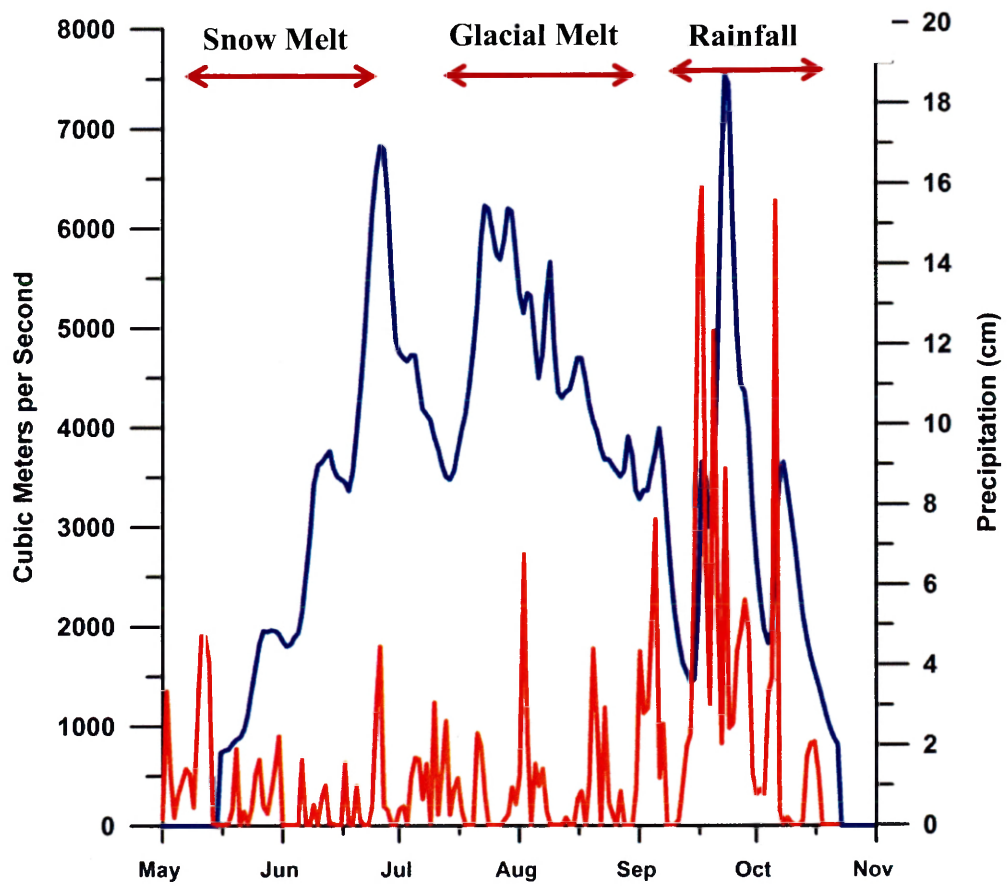


Figure 7. Core P-1 photograph mosaics composed of photos taken immediately after the core was split (right) and after exposure to air overnight (left). The black streaking observed immediately after the core was split was thought to be due to the formation of iron sulfides caused by redox gradients within the core that were driven by varying concentrations of organic matter. The disappearance of this streaking is believed to be the result of oxidation of the core surface after exposure to air.

Core P-1

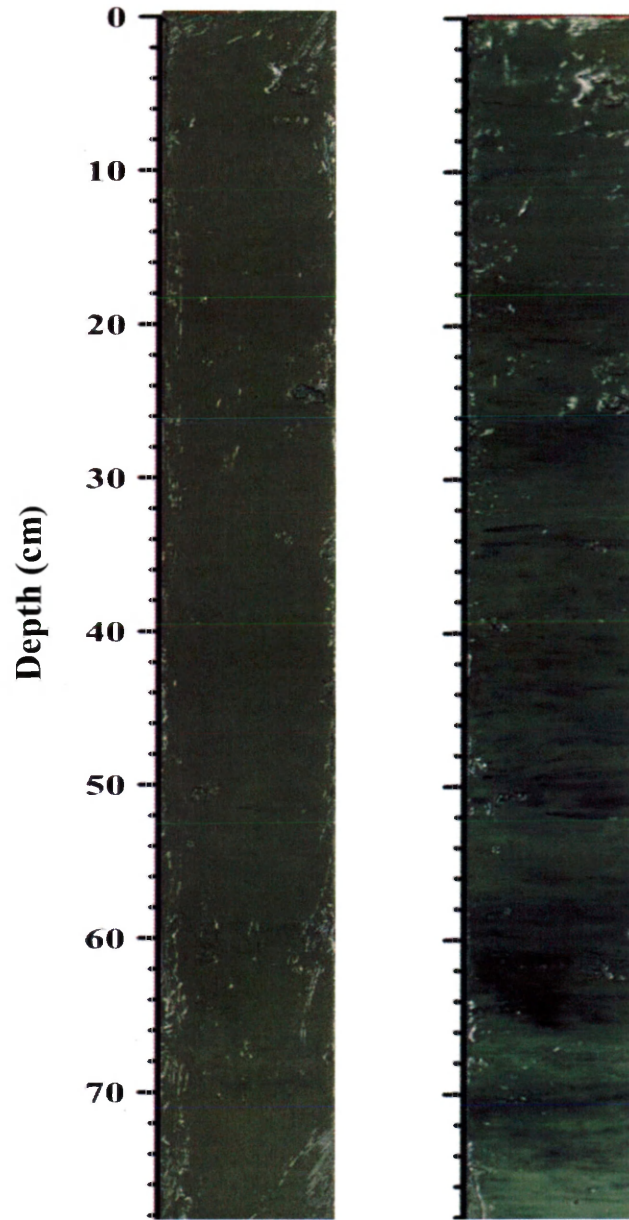


Figure 8. Photograph and x-radiograph mosaics for the transect cores (P-7, P-8, P-9, P-10, and P-12). The physical structure of the cores generally decreased moving northward into the Sound from core P-7 to core P-12.

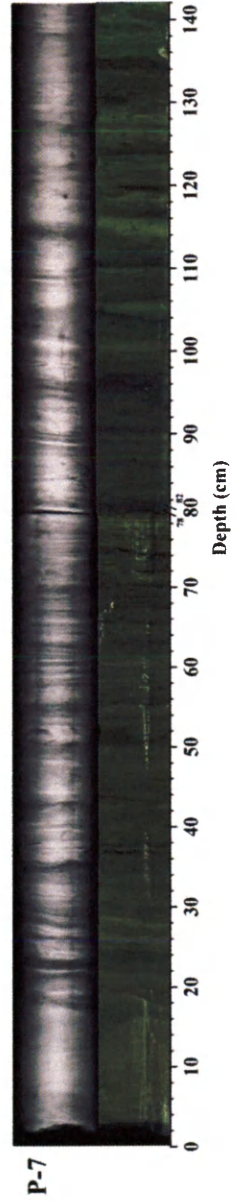
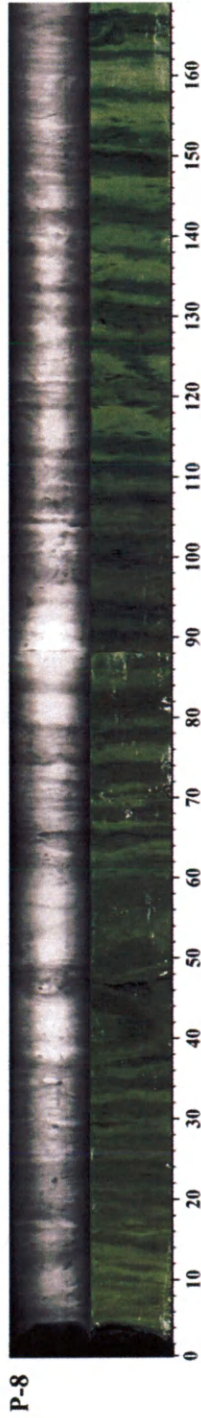
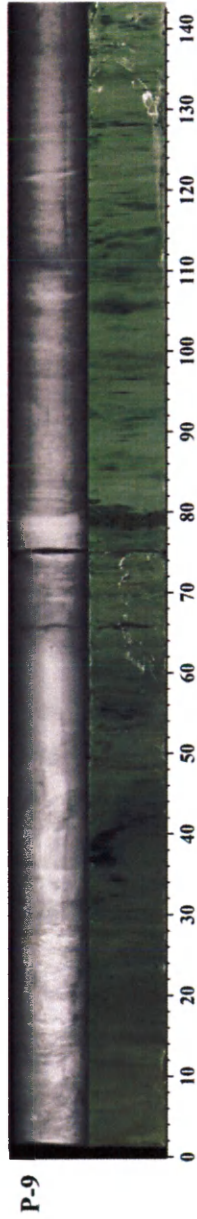
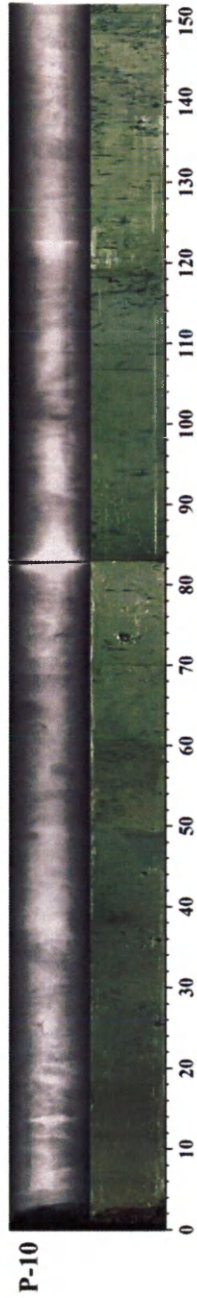
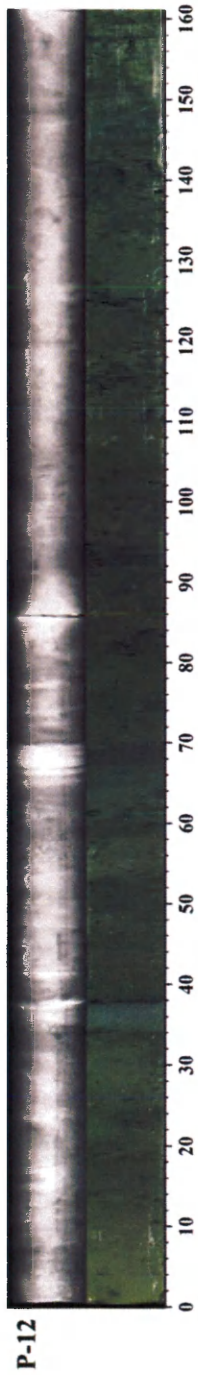


Figure 9. Photograph and x-radiograph mosaics for the non-transect cores (P-1, P-2, P-3, P-5, P-6, P-13). Non-transect cores generally showed mottled textures throughout.

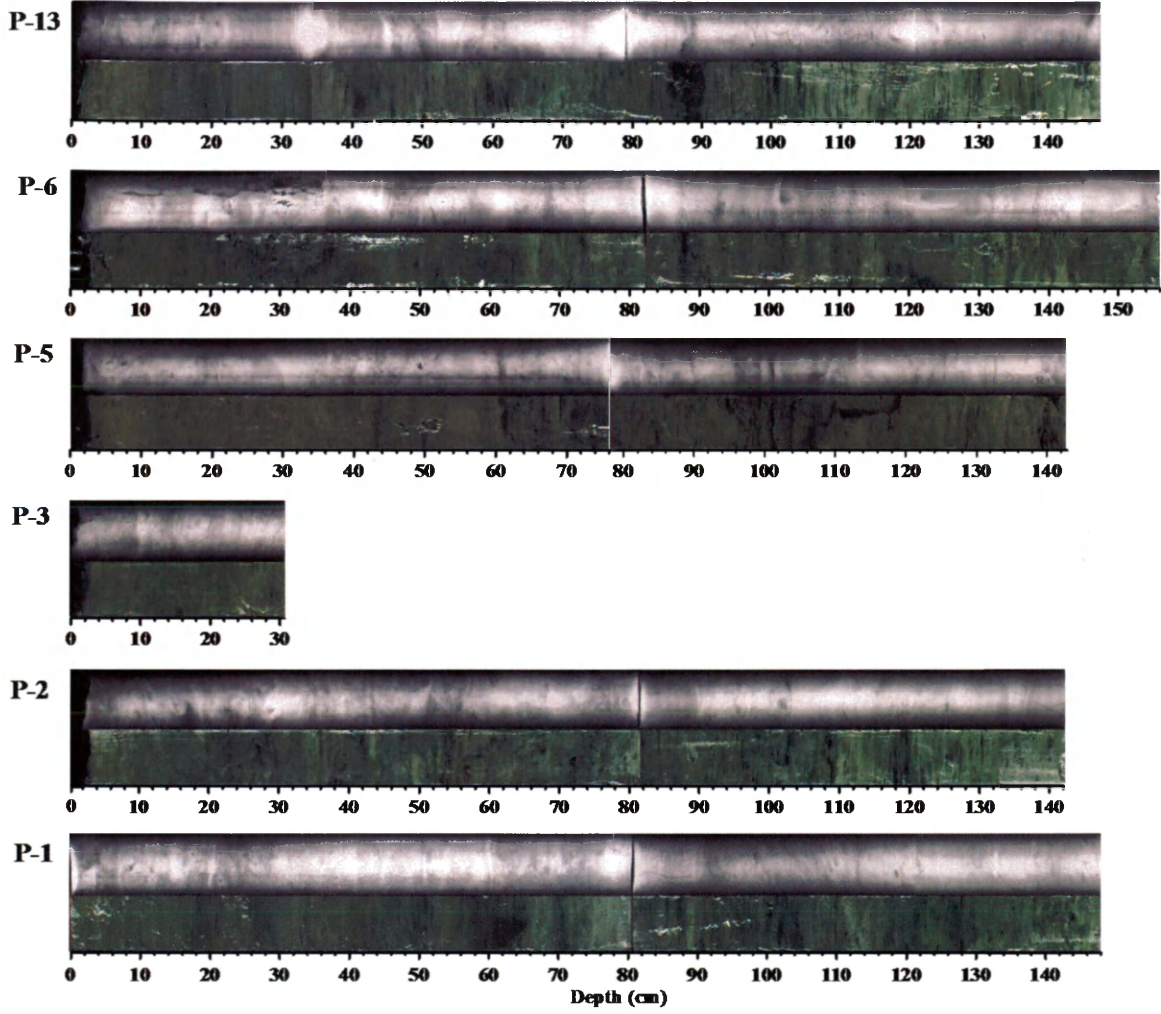


Figure 10. Core averaged percentages of sand and clay sized particles for the central channel transect cores. Relative south-north distance between coring locations represented by the position and spacing on the x-axis. Error bars represent one standard error. From south to north the percentage of sand sized particles decreased while the percentage of clay sized particles increased.

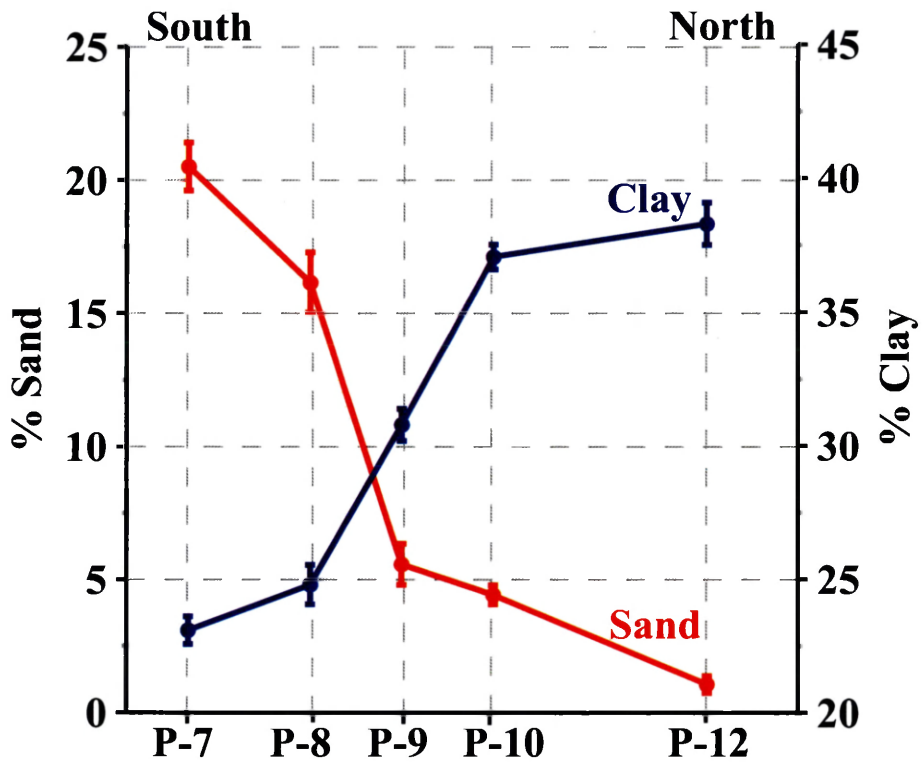


Figure 11. Core averaged percentages of sand (orange), silt (red), and clay (green). In general, cores to the east of the central channel contained lower percentages of sand sized particles. See Table 2 for the standard error associated with the core averaged values.

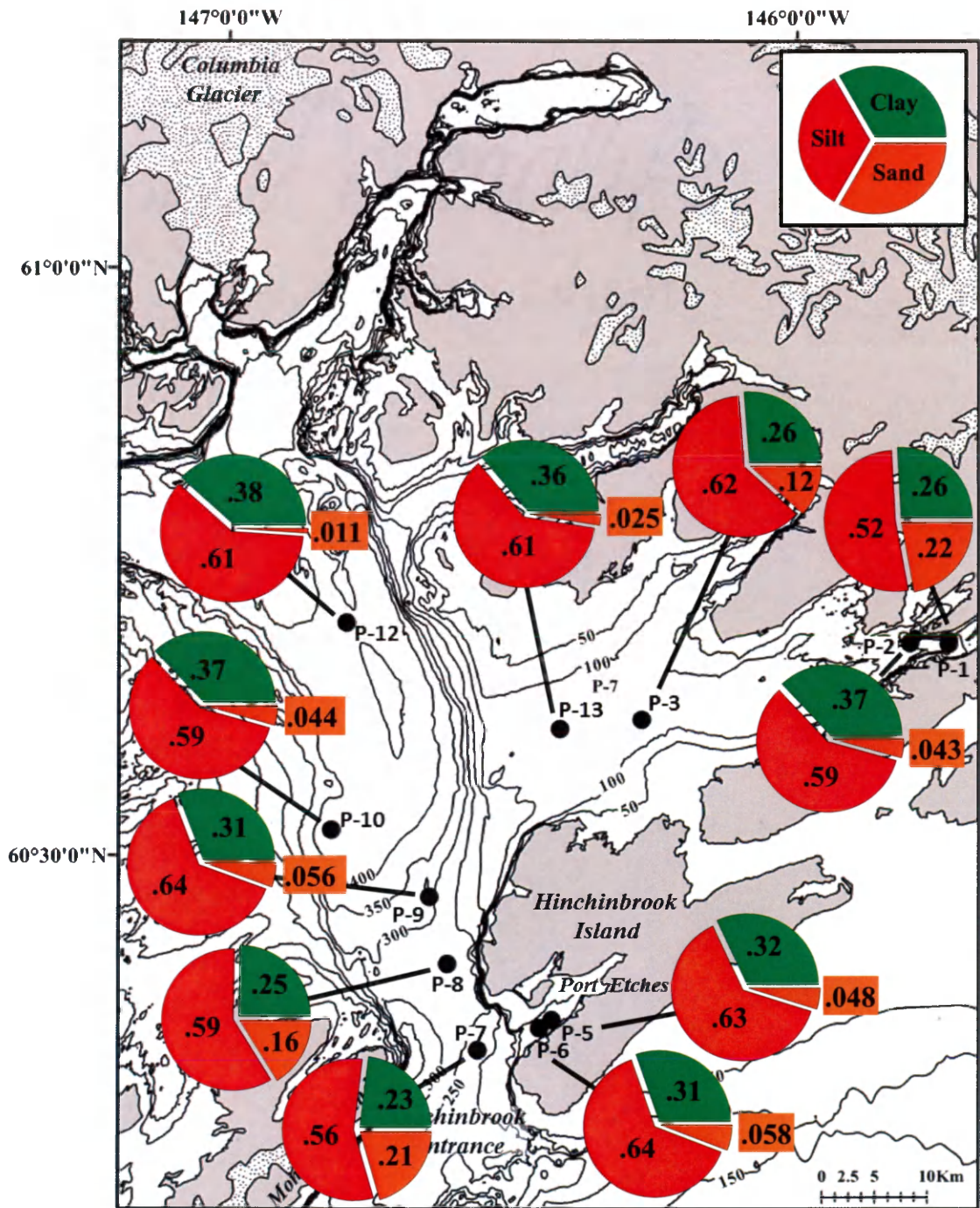


Figure 12. ^{210}Pb (red line) and ^{137}Cs (blue line) derived sedimentation rates for the central channel transect cores. Relative south-north distance between coring locations represented by the position and spacing on the x-axis. Sedimentation rates decreased northward from Core P-7 to Core P-10. From Core P-10 the sedimentation rate increased slightly at Core P-12.

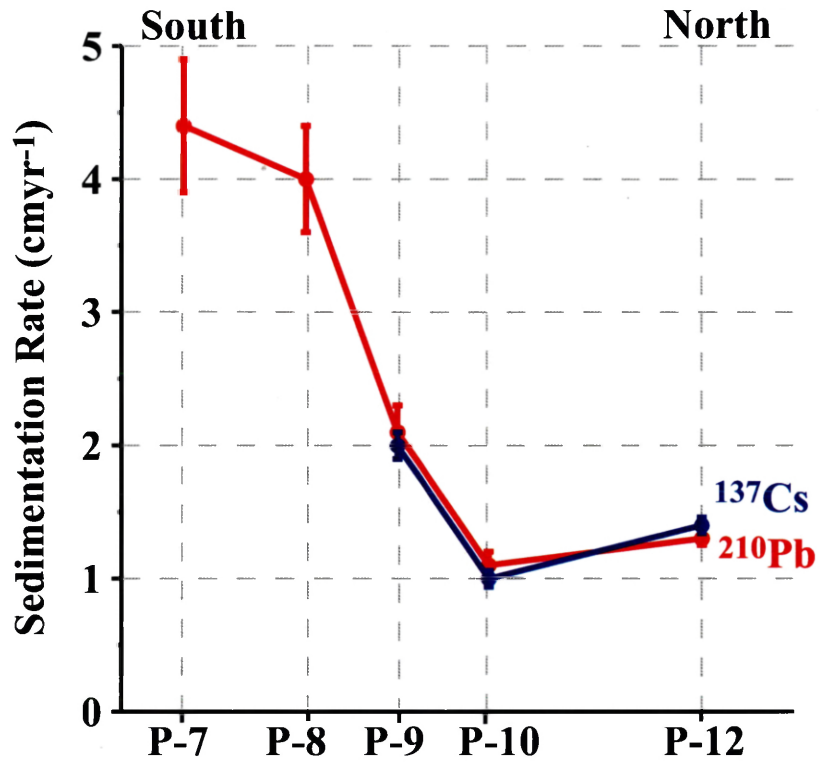


Figure 13. ^{210}Pb (blue) and ^{137}Cs (red) profiles for the Prince William Sound sediment cores. Corresponding ^{210}Pb derived sedimentation rates boxed. In general, rates in the eastern shallow areas of PWS were lower than central channel cores.

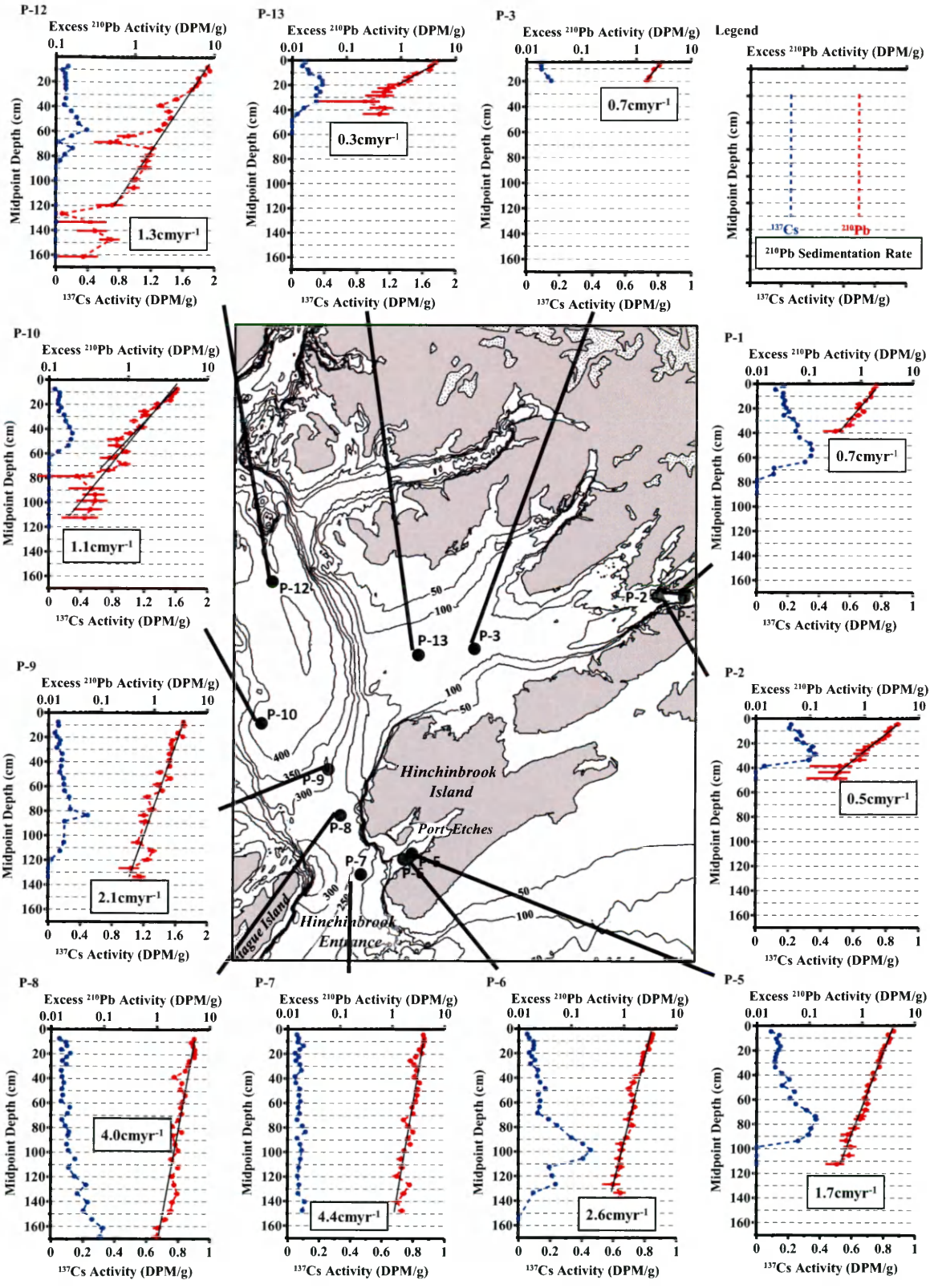


Figure 14. Core P-12 photograph and x-radiograph mosaic with down core XRF Sr/Pb (pink line), Cl (blue line), K (purple line), Ca (yellow line), and K/Ca (orange line) profiles. Peaks in K/Ca observed from 32-38cm, 55-70cm, 120-129cm, and 140-149cm depths corresponded to grey-blue colored sediment in the core photograph and were generally the result of an increase in K and a decrease in Ca.

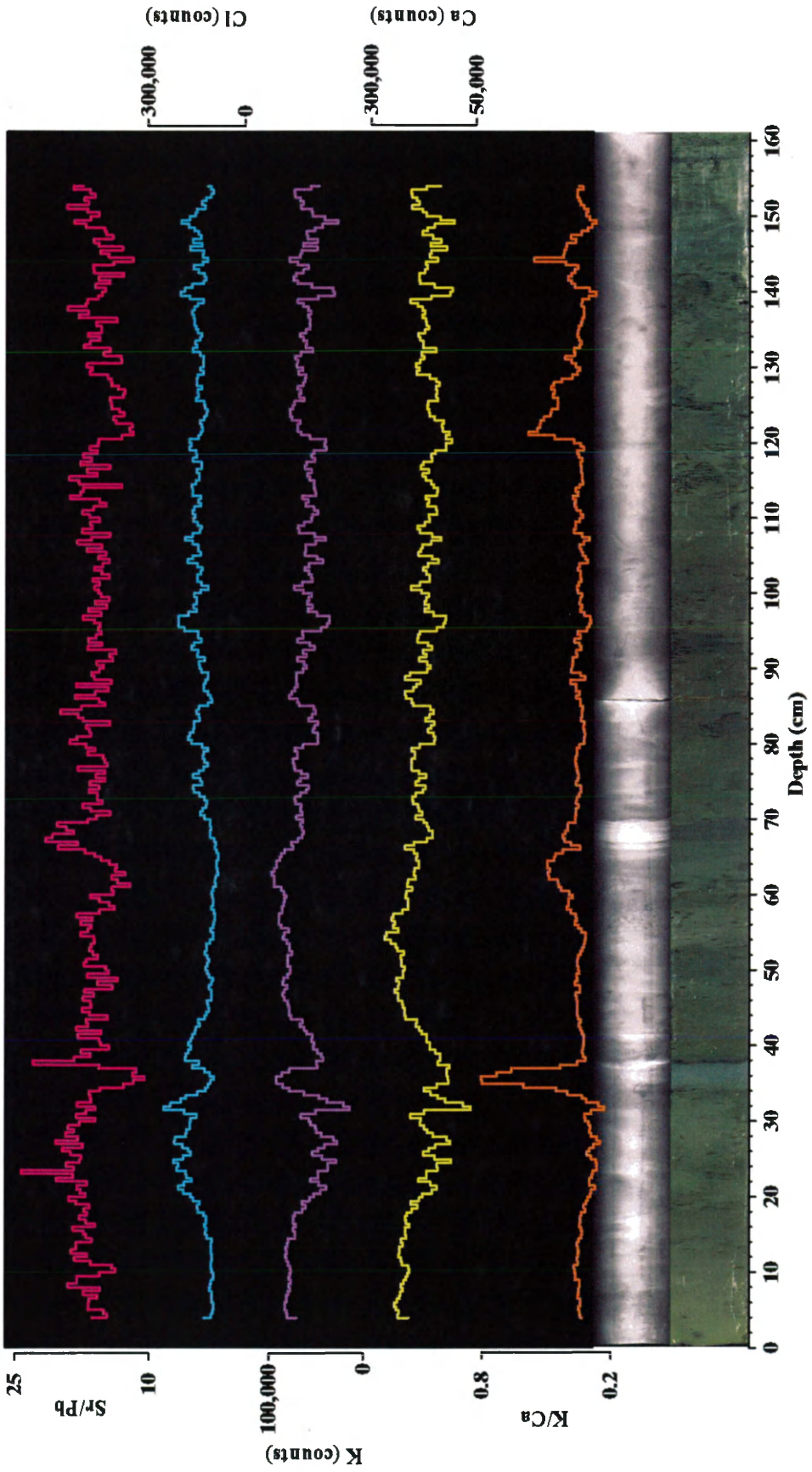


Figure 15. Core P-10 photograph and x-radiograph mosaic with down core XRF Sr/Pb (pink line), Cl (blue line), K (purple line), Ca (yellow line), and K/Ca (orange line) profiles. Peaks in K/Ca observed from 25-28cm and 43-49cm depths corresponded to grey-blue colored sediment in the core photograph and were generally the result of an increase in K and a decrease in Ca.

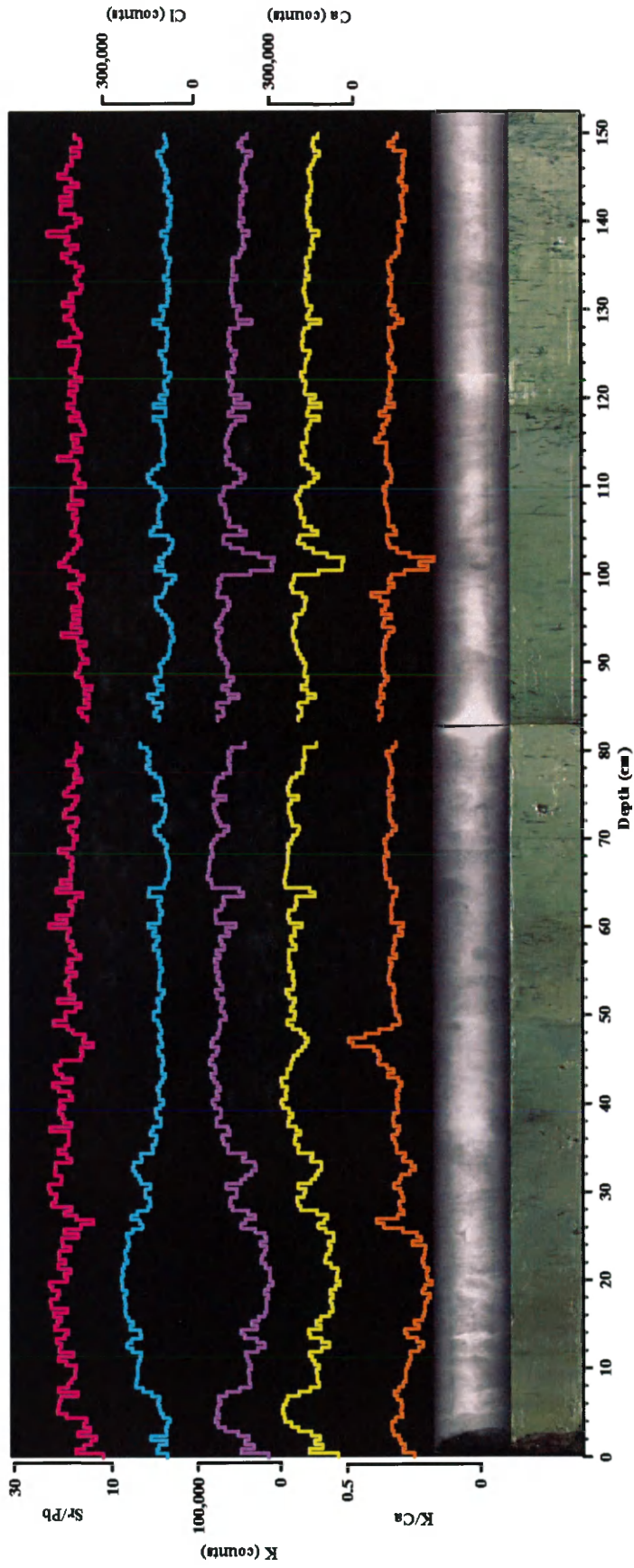


Figure 16. A) Core P-7 photograph and x-radiograph mosaic with the XRF Sr/Pb downcore profile and the percentages of sand, silt, and clay for high resolution subsamples. B) magnified view of high resolution grain size measurements and the corresponding Sr/Pb values. C) relationship between the percentage of sand (upper left), silt (lower left), clay (lower right), mean grain size diameter (upper right) vs. the corresponding XRF Sr/Pb intensities for the high resolution subsamples highlighted in B. The Sr/Pb ratio showed a positive correlation to the percentage of sand and the mean grain size diameter, and a negative correlation to the percentage of silt and clay.

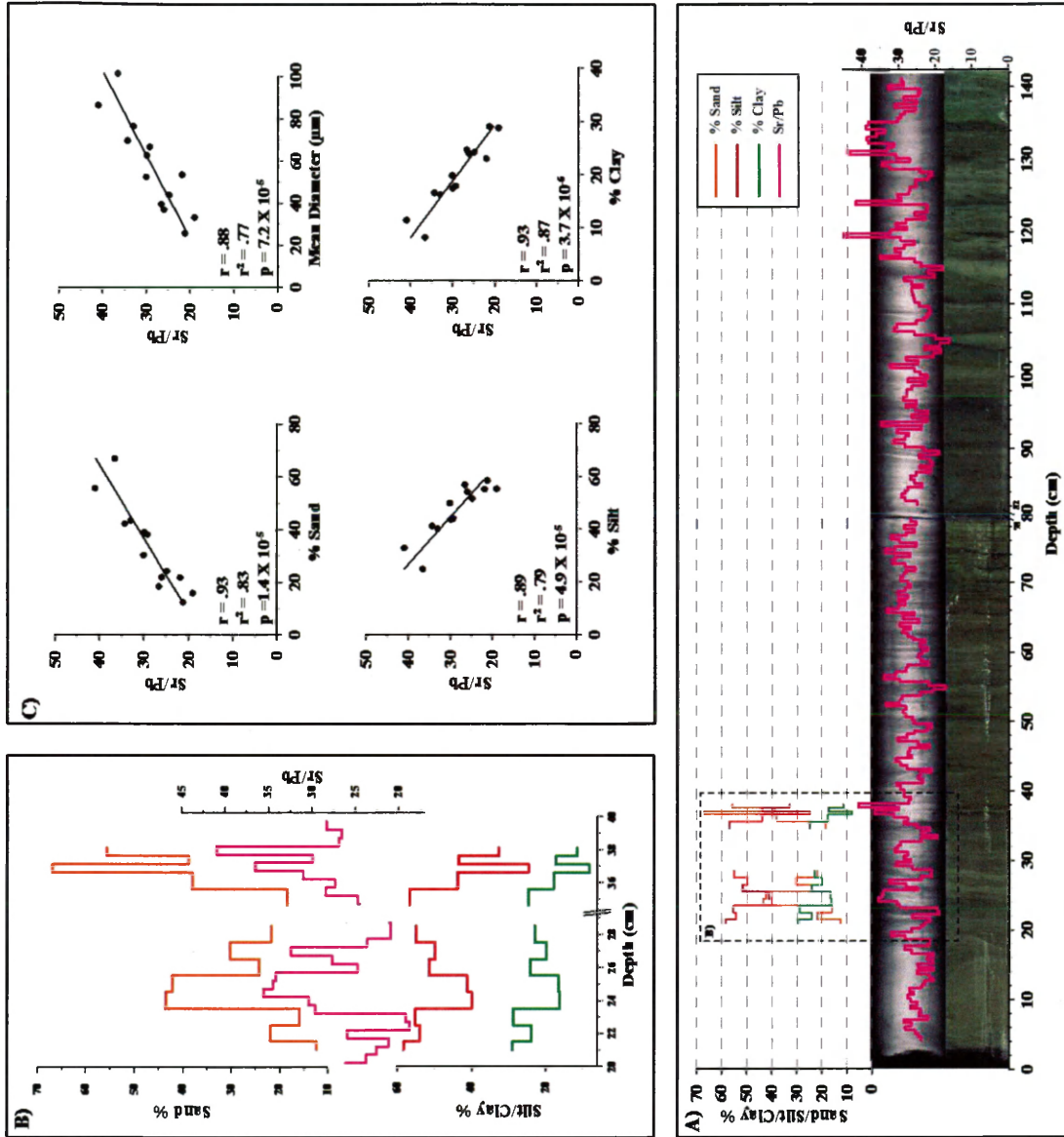


Figure 17. A) Core P-8 photograph and x-radiograph mosaic with the XRF Sr/Pb downcore profile and the percentages of sand, silt, and clay for high resolution subsamples. B) magnified view of high resolution grain size measurements and the corresponding Sr/Pb values. C) relationship between the percentage of sand (upper left), silt (lower left), clay (lower right), mean grain size diameter (upper right) vs. the corresponding XRF Sr/Pb intensities for the high resolution subsamples highlighted in B. The Sr/Pb ratio showed a positive correlation to the percentage of sand and the mean grain size diameter, and a negative correlation to the percentage of silt and clay.

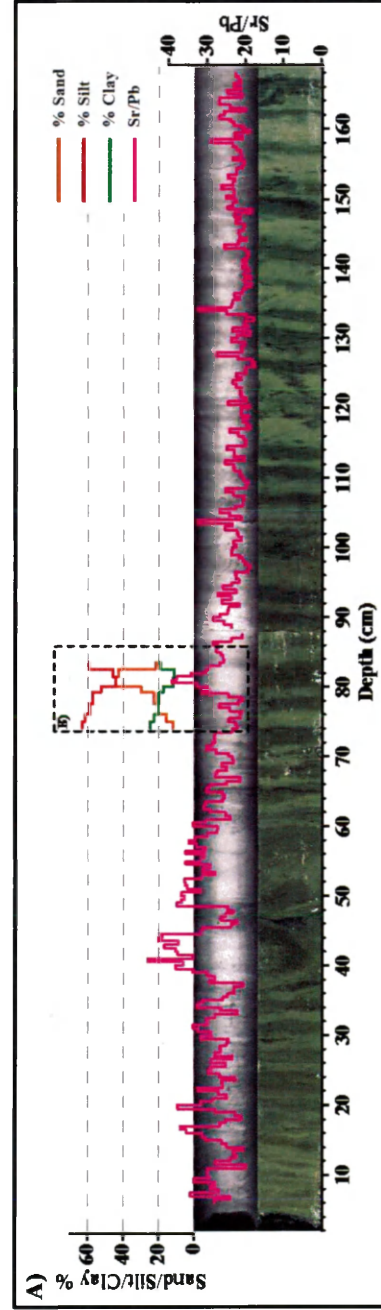
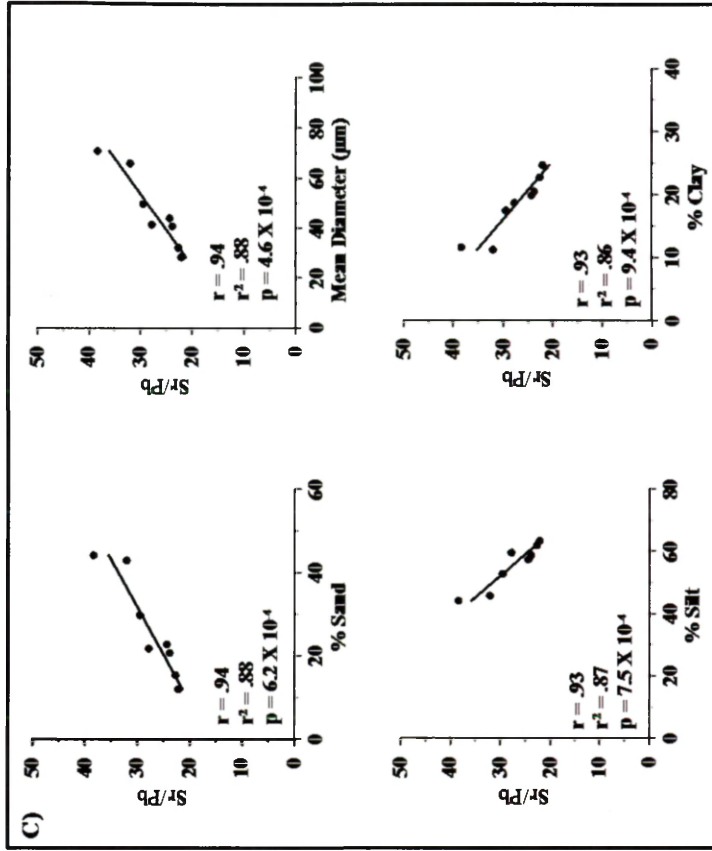
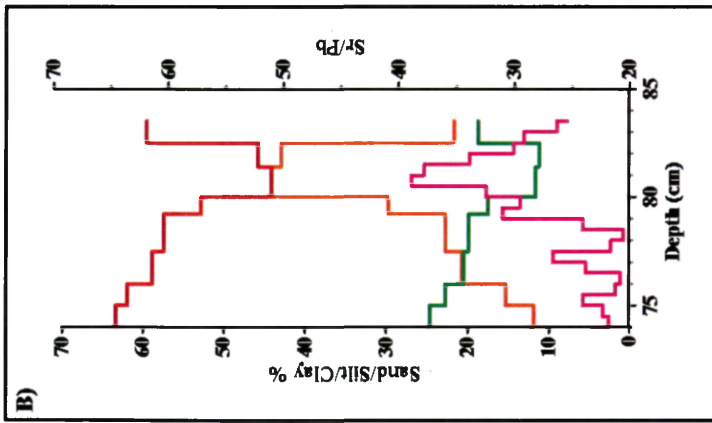


Figure 18. A) Core P-9 photograph and x-radiograph mosaic with the XRF Sr/Pb downcore profile and the percentages of sand, silt, and clay for high resolution subsamples. B) magnified view of high resolution grain size measurements and the corresponding Sr/Pb values. C) relationship between the percentage of sand (upper left), silt (lower left), clay (lower right), mean grain size diameter (upper right) vs. the corresponding XRF Sr/Pb intensities for the high resolution subsamples highlighted in B. The Sr/Pb ratio showed a positive correlation to the percentage of sand and the mean grain size diameter, and a negative correlation to the percentage of silt and clay.

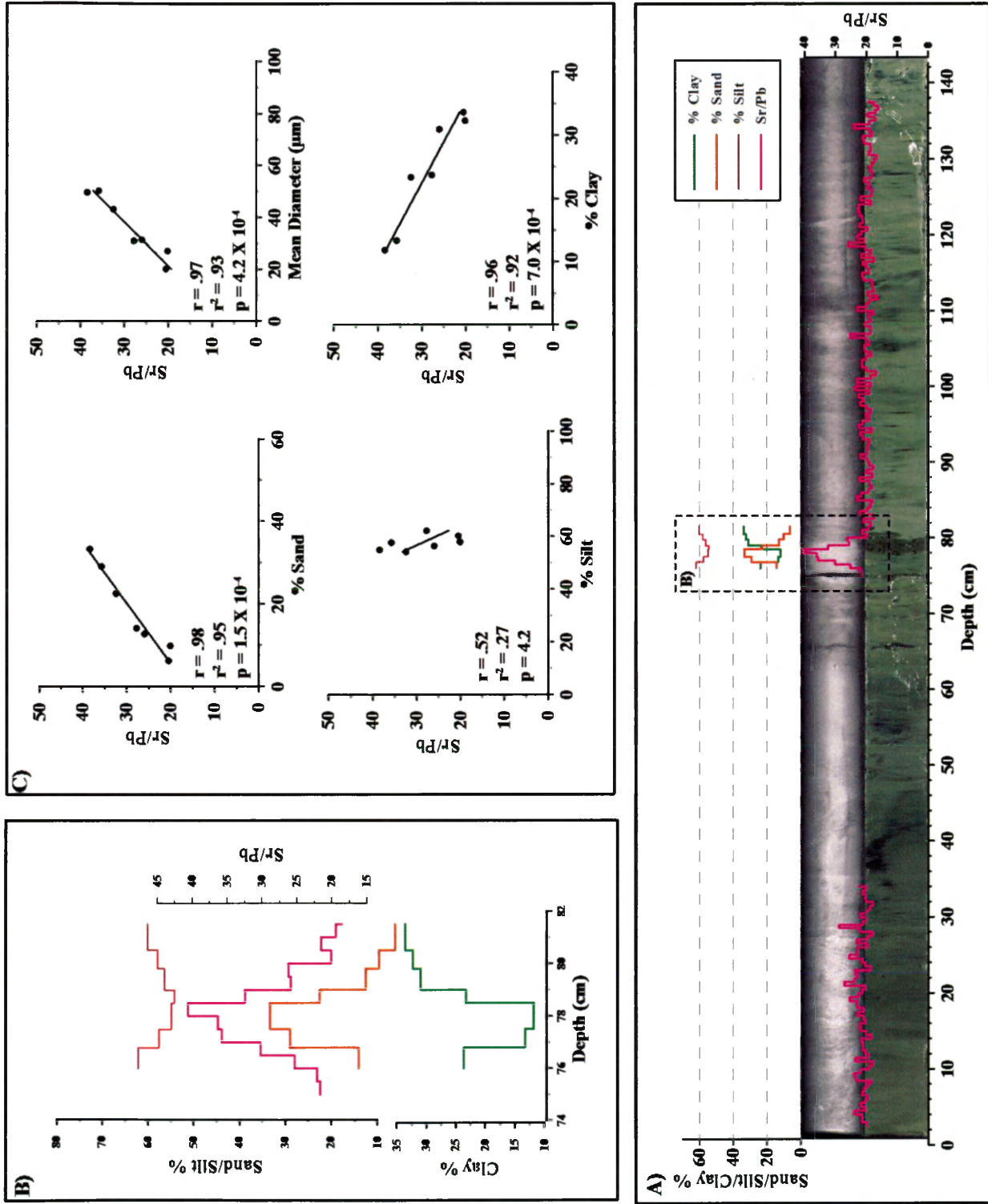


Figure 19. A) Core P-12 photograph and x-radiograph mosaic with the XRF Sr/Pb downcore profile and the percentages of sand, silt, and clay for high resolution subsamples. B) magnified view of high resolution grain size measurements and the corresponding Sr/Pb values. C) relationship between the percentage of sand (upper left), silt (lower left), clay (lower right), mean grain size diameter (upper right) vs. the corresponding XRF Sr/Pb intensities for the high resolution subsamples highlighted in B. The Sr/Pb ratio showed a strong correlation to the percentage of silt and a strong negative correlation to the percentage of clay.

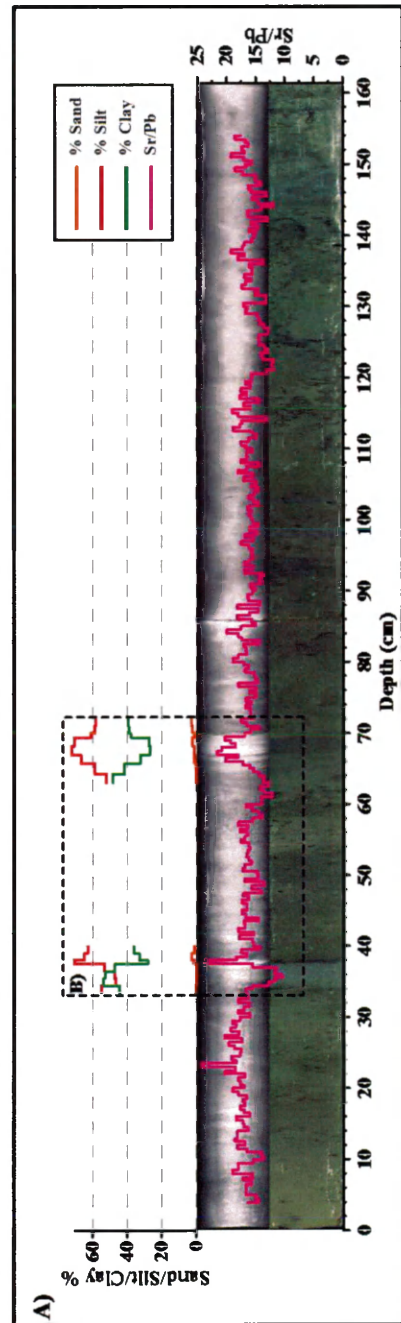
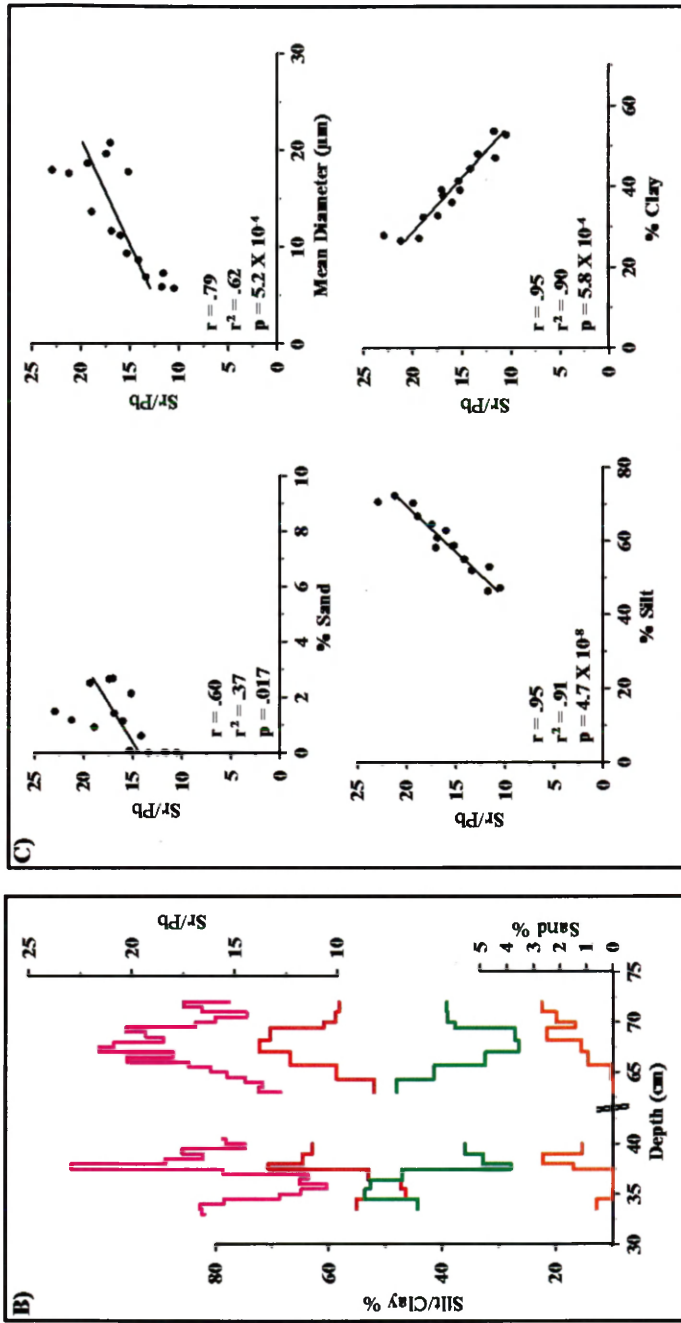


Figure 20. Core P-8 photograph and x-radiograph mosaic with the smoothed (3 point running averaged) Sr/Pb (pink like), Cl (blue line), and Br/Cl (green line). In the upper 90cm of the core the Br/Cl ratio was significantly influenced by water content (Cl) which appeared to be driven by high Sr/Pb, sandy layers. At depths greater than 90cm high Sr/Pb, sandy layers are not observed and peaks in the Br/Cl ratio generally correlated to the dark colored redox laminations.

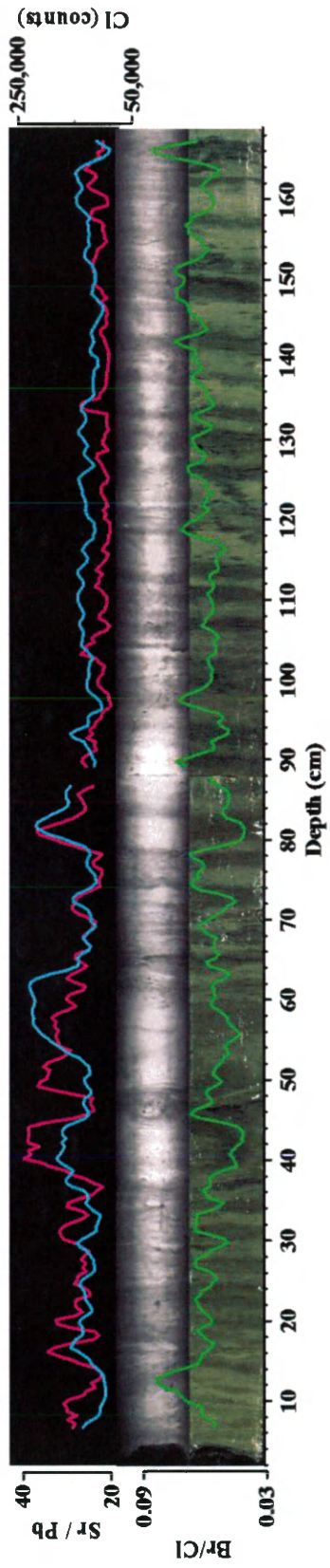


Figure 21. K (top) and Ca (bottom) concentrations for the Prince William Sound and Copper River basins (outlined in black) interpolated from streambed sediments collected and analyzed by the United States Geological Survey (USGS). Generalized location of Columbia Glacier (CG) shown by the dashed black line. In general, the Columbia Glacier region of Prince William Sound was relatively enriched in K and depleted in Ca relative to the Copper River basin. Modified from the USGS, 2013.

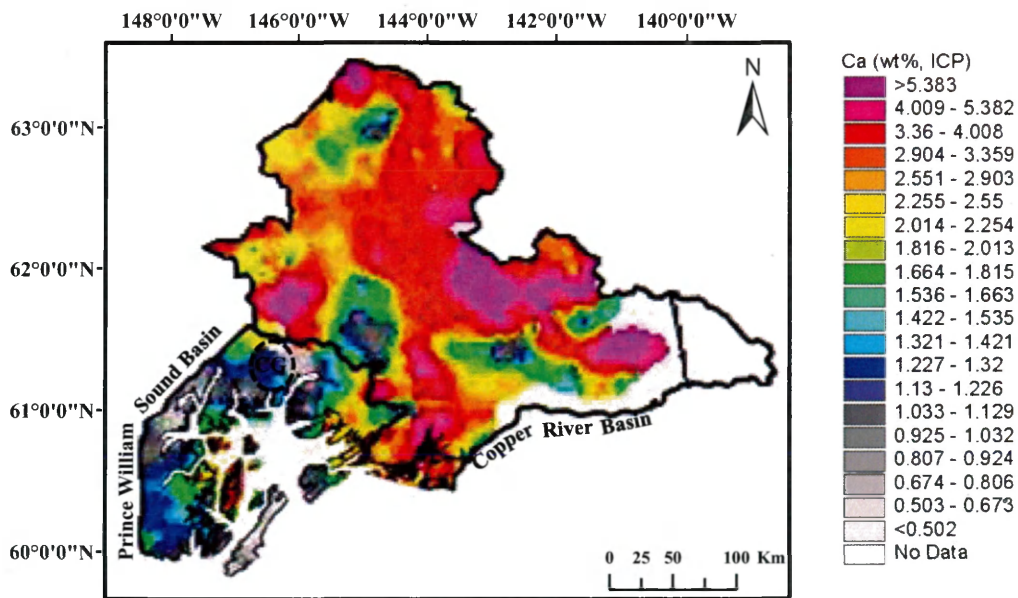
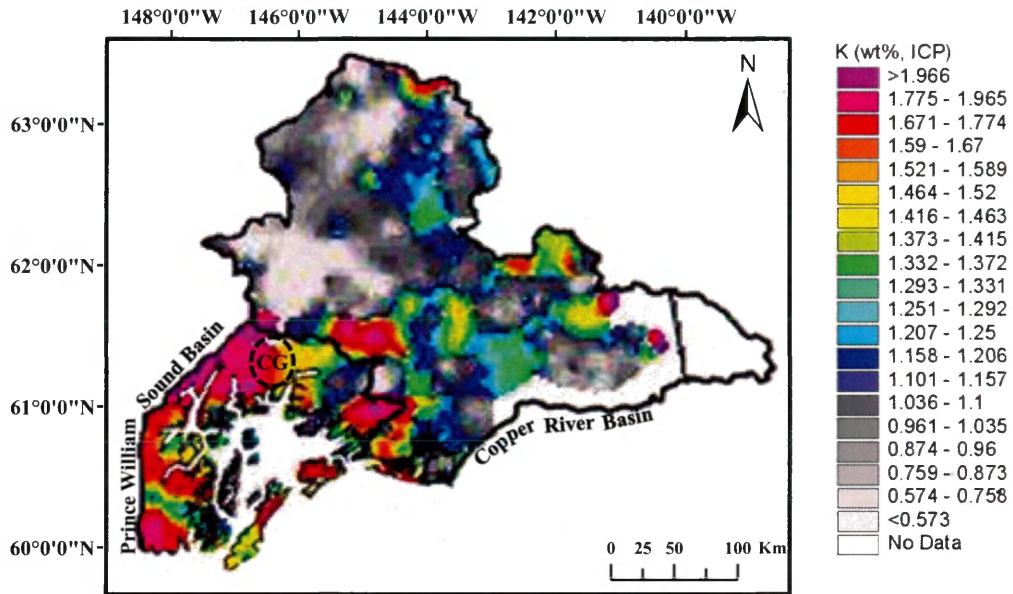


Figure 22. Epicenters for the potential earthquakes that caused the gravity flow deposits in the Prince William Sound sediment cores (P-9, P-10, P-12, P-13). Dates and magnitudes (M) labeled on map. Data obtained from the USGS, 2014B.

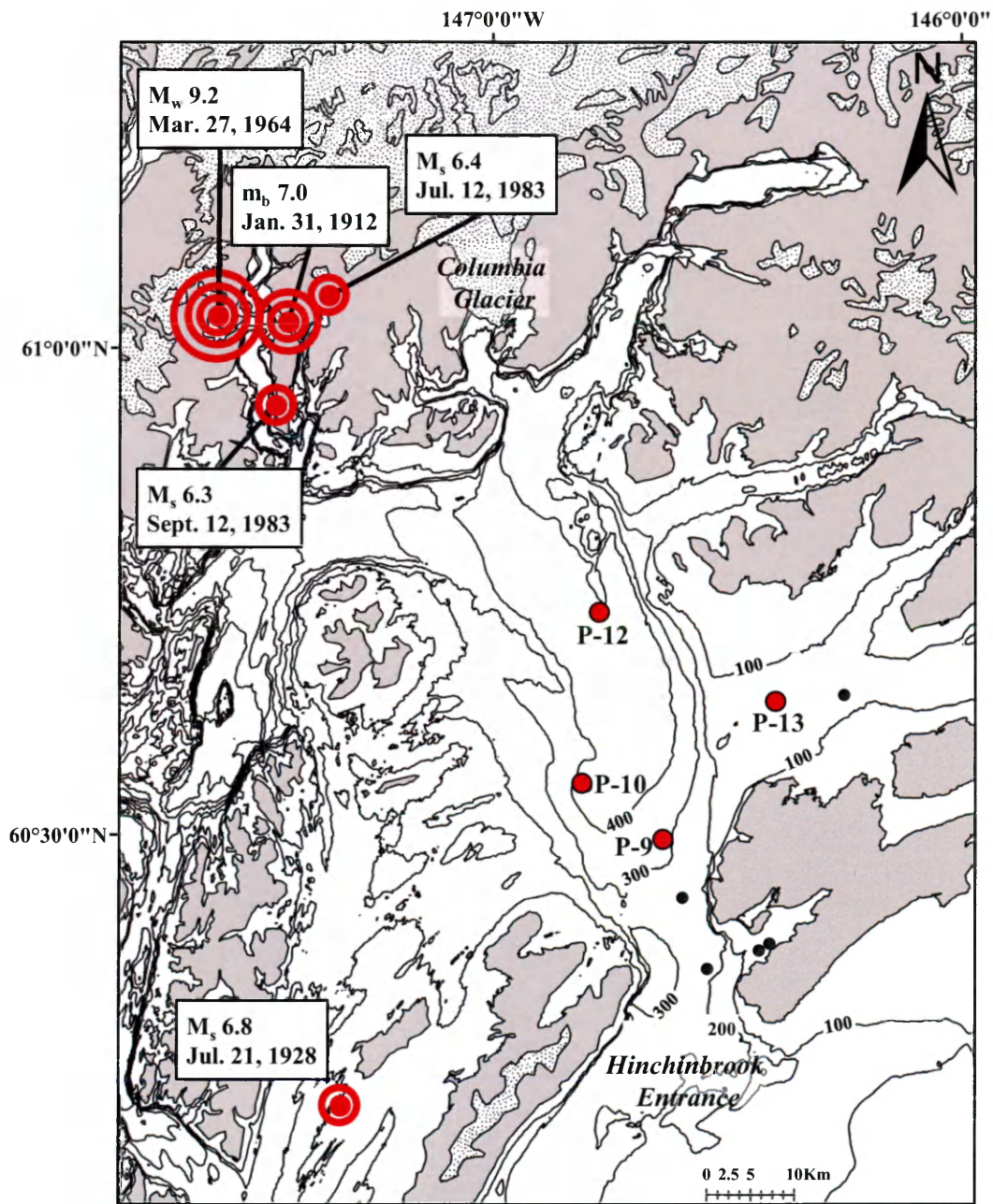


Figure 23. Core P-9 photograph and x-radiograph mosaic with down core XRF Sr/Pb (pink line), Cl (blue line), K (purple line), Ca (yellow line), and K/Ca (orange line) profiles. The missing Sr/Pb profile from 36-76cm was due to an instrumental error during the 30kV scan. The gravity flow deposit that has a base at 80cm did not display a peak in K/Ca similar to the gravity flow deposits in Cores P-10 and P-12.

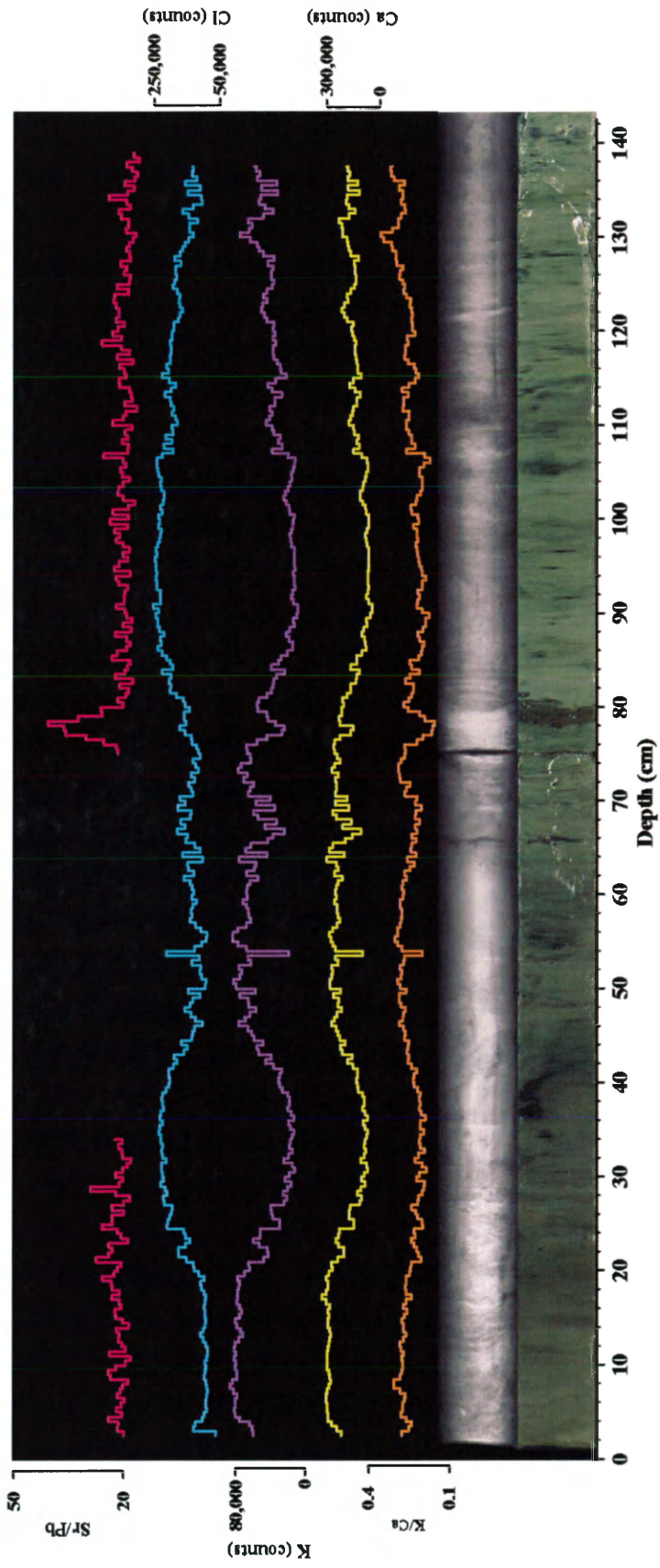


Figure 24. Core P-13 photograph and x-radiograph mosaic with down core XRF Sr/Pb (pink line), Cl (blue line), K (purple line), Ca (yellow line), and K/Ca (orange line) profiles. The gravity flow deposit that has a base at 34cm did not contain and a peak in the K/Ca ratio similar to the gravity flow deposits in Cores P-10 and P-12.

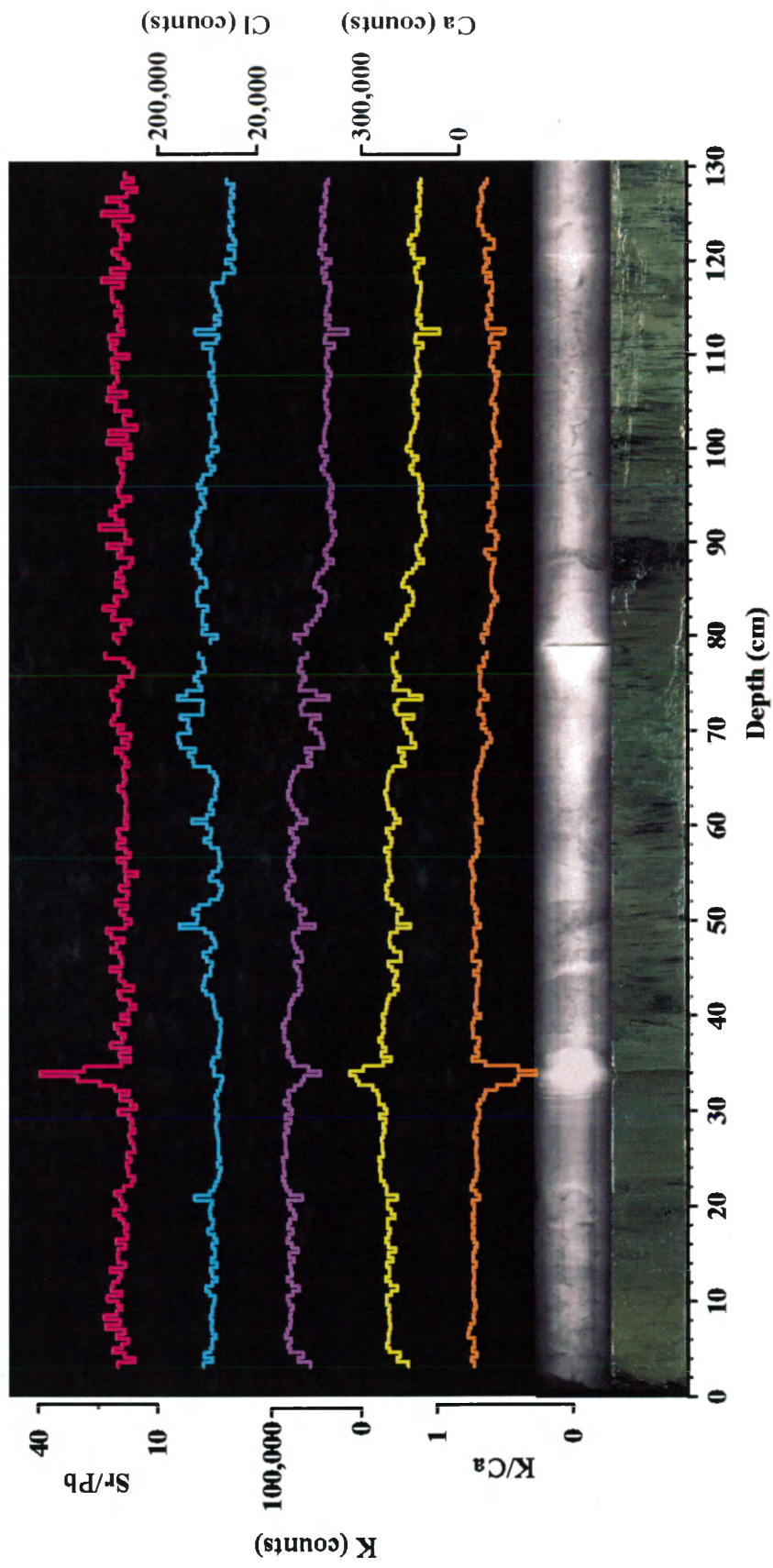


Figure 25. Lake levels of Lake Kadin (top) and Lake Terentiev (bottom) from 1976-2000 as determined by aerial altimetry. During this time period there have been many outburst events which are shown by a rapid decrease in lake level. From Kimmel (2001).

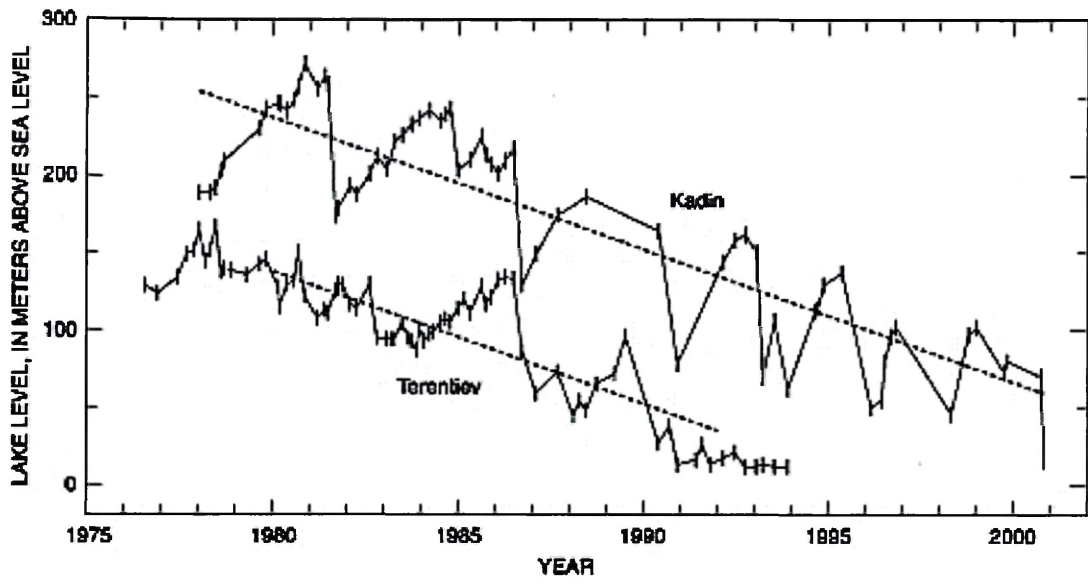


Figure 26. Core P-7 photograph and x-radiograph mosaic with the Sr/Pb down core profile (pink line). Dashed lines separate the Sr/Pb cyclicity into “annual deposits” determined by visual interpretation. Dominate periods (cm) determined by FFT analysis of Sr/Pb values for 96-128cm (top-right), 60-92cm (top-middle) and 28-60cm (top-left) intervals. From 96-128cm, the dominate FFT period of 4.6cm agrees well with both the core averaged sedimentation rate of $4.4\text{cm}\text{yr}^{-1}$ and the thickness of visually determined deposits (4.0 - 5.0cm) for the same interval.

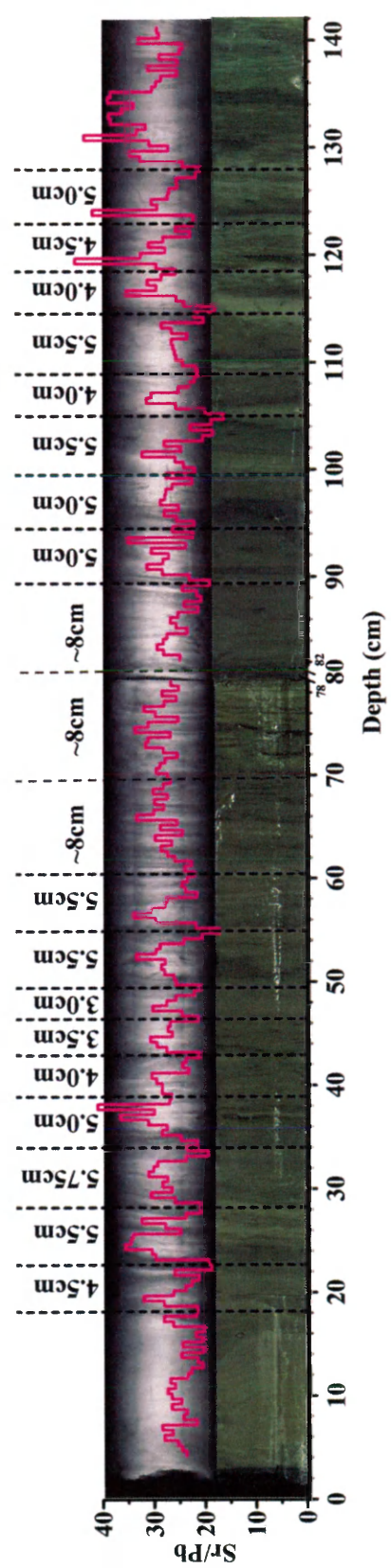
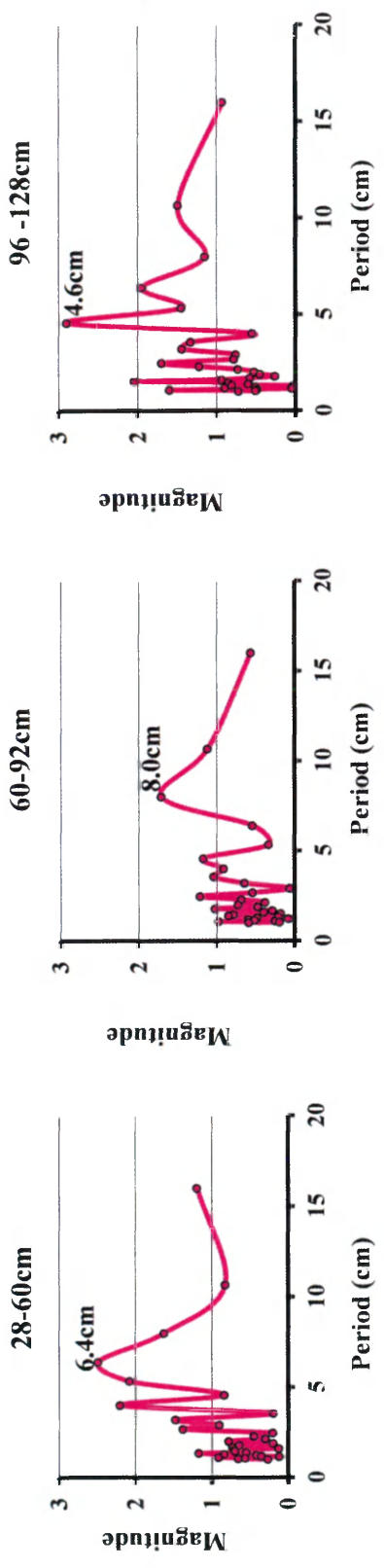


Figure 27. Core P-8 photograph and x-radiograph mosaic with the down core Br/Cl profile (green line). Visually interpreted “annual deposits” based on redox banding shown by dashed lines. These deposits ranged in thickness from 3.5-8.0cm, with an average thickness of 5.0cm, which is slightly higher than the core averaged sedimentation rate of 4.0cm yr^{-1} .

